POLITECNICO DI TORINO

Corso di Laurea Magistrale in

Ingegneria Aerospaziale

Tesi di Laurea

Low-speed airfoil noise simulation

DNS post-processing on a Controlled-Diffusion airfoil

Relatore
Prof. Renzo Arina

Candidato
Susanna Orestano

Ottobre 2019

All'Hacker,
dalla tua cita

Acknowledgements

Nonostante mi sembri ancora incredibile, sembra sia giunto il momento di porre fine al mio percorso universitario. Terminare questa tesi rappresenta il raggiungimento di un obiettivo che mi sono posta nel lontano maggio di sei anni fa, ancora inconsapevole della miriade di esperienze a venire.

Vorrei, innanzitutto, ringraziare il mio relatore, il Professor Renzo Arina, per la sua estrema disponibilità e per avermi aiutata nelle peripezie burocratiche che ha comportato l'Erasmus. Ringrazio inoltre i Professori Michel Roger e Stéphane Moreau, per avermi introdotta all'aeroacustica e per avermi accolta nei loro laboratori di ricerca.

Voglio condividere questo successo con te, Ciaccia, un piccolo tassello del futuro che abbiamo tante volte immaginato e che ci sembrava lontano ed irraggiungibile. Ci siamo riuscite, ci credi? Grazie per scegliere ogni giorno di ascoltare questa figlia un po' folle, sono fiera di noi e di ciò che siamo diventate. Non finirò mai di esserti grata per avermi capita e sostenuta nonostante la distanza e gli innumerevoli fattori esterni che hanno reso questo percorso così tanto arduo. Qualcuno ci disse che la nostra forza sarebbe stata lo stare *sempre 'nsema*: aveva ragione.

Grazie, Nonna, per le tue telefonate: anche se la tua nipotina scappa dall'altra parte del mondo ti porta sempre nel cuore.

Ringrazio i miei amici, che hanno scelto di rimanere nonostante i kilometri che ci dividono aumentino di anno in anno. Manny, perchè la tua buonanotte è sempre una certezza e perchè ogni volta che ti rivedo sembra sia passato mezzo secondo dalla volta precedente; sono certa che le gioie siano in avvicinamento, non può piovere per sempre. Mauri, per aver sopportato le mie ansie e per riuscire a farmi ridere come a lezione, nonostante qualche oceano di troppo. W, perchè ti sei lasciata affascinare dalla Francia e perchè dimostri di volermi bene, pur conoscendomi come le tue stesse tasche. E infine Occhibbelli, per farmi sentire a casa ogni volta che rimetto piede a Torino.

Merci Hao, pour ta compagnie et pour l'été merveilleux qu'on a passé ensemble. Et finalement merci Ciciri, pour supporter cette petite italienne surexcitée qui est rentrée dans ta vie pendant un après-midi centralien. J'ai hâte de vivre (ensemble) la suite.

Résumé du rapport:

La prédiction du bruit de bord de fuite émis par un profil à diffusion contrôlée à un angle d'attaque de 8° a été évaluée, en repartant des travaux d'un post-doctorat précédemment effectué à l'Université de Sherbrooke. Ce profil a été conçu pour des applications à basse vitesse. Deux types de simulation numérique ont été comparés: une simulation directe fondée sur la résolution des équations de Navier-Stokes et une autre qui exploite la méthode de Lattice-Boltzmann. Les données de trois sondes positionnées sur l'extrados du profil ont été considérées.

Les bases théoriques de la turbulence ont été rapidement présentées ainsi que les méthodes numériques utilisées. La prédiction du bruit exploite dans ce cas la théorie d'Amiet pour le bruit de bord de fuite et le modèle statistique anisotropique de Panton et Linebarger pour la modélisation des sources. Pour cela, une caractérisation de la couche limite ainsi qu'une analyse des statistiques de la turbulence ont été effectuées pour les deux types de simulation. La prédiction du bruit a été calculée à l'aide de deux méthodes Monte Carlo: l'échantillonnage récursif stratifié et l'échantillonnage préférentiel.

Mots-clés libres: aéroacoustique ; Amiet ; brut de bord de fuite ; large-bande ; turbulence ; numérique ; CAA ; modèle statistique ; Monte Carlo

Abstract:

The trailing-edge noise prediction for a Controlled-Diffusion airfoil at an angle of attack of 8° have been evaluated by starting from the work of a previous post doctoral researcher at Sherbrooke University. Two types of numerical simulation have been compared: a direct numerical simulation based on Navier-Stokes equations and another one which exploit the Lattice-Boltzmann method. Data from three sensors on the suction side of the airfoil have been considered.

The theoretical basis of turbulence and the considered numerical methods have been briefly presented. In this case, the noise prediction exploits Amiet's theory and the statistical anisotropic Panton and Linebarger model for source modeling. For this reason, a boundary layer characterisation and an analysis of turbulence statistics has been carried out for the two kinds of simulation. Noise prediction has been computed through two different Monte Carlo methods: the recursive stratified sampling and the importance sampling.

Keywords: aeroacoustics ; Amiet ; trailing-edge noise ; broadband ; turbulence ; numerical ; CAA ; statistical model ; Monte Carlo

Contents

List of Figures

1

Introduction

Sherbrooke University has been founded in 1954. The Department of Mechanical Engineering, created a year later, welcomes 400 new students every year. Moreover, around 80 students attend there masters or PhDs. The research carried out by the aeroacoustics group focuses on the characterisation of the acoustic radiation in fluids, on active and passive noise control methods and to aeroacoustics applied to turbo-engines.

The Center for Acoustic Research at Ecole Centrale de Lyon was created in the 1980s to meet the growing interest in aeroacoustics and in the interaction between acoustics and turbulent flows. It is part of the Fluid Mechanics and Acoustics Laboratory (LMFA) and of the Fluid Mechanics, Acoustics and Energy Department (MFAE). The activities of the Center for Acoustic Research are organized around aeroacoustics of rotating surfaces, dynamic and acoustic of compressible shear flows and propagation in non-homogeneous media and non-linear effects.

The internship was carried out in both research groups. The project focuses on the study of wall-pressure fluctuations at the trailing edge of an airfoil and on the effect of boundary-layer pressure gradients. A significant amount of experimental and numerical data has been collected during PhDs in both universities. The internship aims at validating the wall-pressure fluctuations prediction of previous PhDs.

This report firstly presents the internship background and the interest of airfoil noise reduction. A brief overview about the theoretical concepts of turbulence is then provided. The state-of-art of empirical and analytical models to compute wall-pressure spectra and acoustic propagation are addressed too, with a particular focus on the numerical computation techniques. In the last section, a case study for Direct Numerical Simulation is presented, along with a description of the obtained post-processing results.

1.1 Interest of airfoil noise reduction

Aerodynamic noise is the most common by-product of rotating machines or airframes operating in a flow. As the sound is generated within the acoustic medium, the complexity of measurement and analysis is considerable. For instance, the noise generated by wind turbines in the proximity of inhabited areas is still a contentious issue. The sound level perceived at distance depends on countless factors, which make its prediction complicated. Another domain affected by this problem is aviation. The majority of sound is produced by the motion of air and its interaction with the solid boundaries of the aircraft structures.

Over the last 30 years, the development of air transport systems and consequently the increase of air traffic generated an enhanced focus on noise levels. Governments have enacted more and more legislative controls about this environmental concern. Noise is produced by aircraft engine propellers, fans, combustion chambers and external surfaces and have a strong impact on the health of people living in exposed areas. Aircraft noise has been progressively reduced through flight paths and traffic optimisation, but directly dealing with its sources still represents a research challenge. Starting from Lighthill's pioneering work in 1950s, many attempts to find a mathematical approach to explain noise generation and to develop noise reduction methods have been made.

Airfoil trailing-edge noise or self-noise remains one of the main noise sources for low speed fans. It represents the minimum noise level produced by a machine in a configuration free of any interaction with other components. This sound is produced by the re-organisation of vortices carried by boundary layer when meeting a singularity: the trailing edge of the blade profile. As a matter of facts, vorticity distortions and boundary-layer turbulence scattering produce acoustic waves, propagating upstream and downstream. Two kinds of noise can be observed:

- *tonal noise*: if the boundary layer is transitional. Strong acoustic tones can be present in the sound spectrum, 20 - 30 dB higher than broadband noise. Acoustic disturbances are produced by the interaction between vortices and the geometrical discontinuity of trailing edge (ROGER and MOREAU 2004). Numerical simulations proved the existence of a feedback mechanism: sound waves produced at trailing edge and propagating upstream blend with the original disturbance. Recent research stated that both suction and pressure side feedbacks may contribute to noise. The generation of this phenomenon has been deeply analysed for analytical and numerical work. Most of the studies agree on a feedback-loop mechanism at the basis of frequency selection and tonal noise, but it is still an active debate.

- *broadband noise*: if the boundary layer is turbulent. When it is also detached from trailing-edge (TE) a higher lower frequencies content can be noticed. A turbulent flow is characterised by random changes in pressure and velocity. It is composed by eddies of various sizes, constantly moving with no preferential direction. This creates surface pressure fluctuations which generate acoustic waves at TE. Unlike tonal noise, the physical insight of broadband noise generation has already been further explained. However, some topics such as the role of Kutta condition still need to be clarified. Eventually, numerically resolving the small scales of turbulence to analyse this kind of noise is challenging. High Reynolds numbers are required, implying a huge computational cost.

1.2 Objectives of the internship

The trailing-edge self-noise was firstly studied through experimental approaches. Even is the experiments remain a fundamental tool for research, the analytical and numerical studies play a more and more important role in this domain. This internship project exploits Direct-Numerical Simulation (DNS) data of a previous PhD in Sherbrooke University (see (WU 2019), (SANJOSE and MOREAU 2011)) to investigate wall-pressure fluctuations. The case study is a Controlled-Diffusion airfoil at high Reynolds number based on the chord. The objectives of the internship are the following:

1. Validate the wall-pressure fluctuations prediction methods exploited during previous research for two sensors on a Controlled-Diffusion airfoil

2. Apply the same methods to different sensors on the airfoil surface for sake of comparison

3. Compare two types of numerical simulations (Navier-Stokes and Lattice-Boltzmann method DNS) for the same case study

4. Analyse the effect of adverse pressure gradient on the airfoil and of boundary layer anisotropy

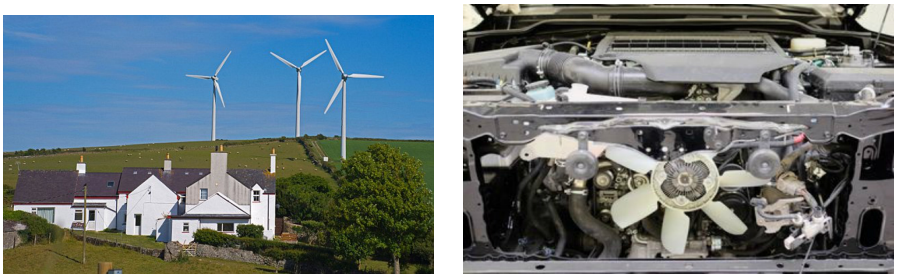

(a) (b)

Figure 1.1: Some examples of domains which require noise reduction.

2

Theoretical prerequisites and state-of-the-art

Researches on the trailing-edge noise started in the late 1970s. Initially based on theoretical models and experimental measurements, they addressed wall-pressure fluctuations and far-field sound. The introduction of numerical methods over the past few decades has broadened the field of research. Experimental data collected in previous studies are used now as a validation tool for numerical simulations. The following section introduces firstly some turbulence fundamentals related to the current study. Secondly, acoustic analogies involving different wall-pressure fluctuations modeling and far-field sound radiation will be addressed. Eventually, the application of acoustic analogies to numerical simulations will be covered.

2.1 Turbulence overview

Figure 2.1: A turbulent cascade as seen by Leonardo da Vinci.

Similar measurements on a laminar flow with the same set of initial and boundary conditions yield similar results. This is, however, not valid for the

case of turbulent flows: turbulence is not deterministic and must be analysed from a statistical point of view. (CHASSAING 2000) In the specific case of a homogeneous turbulent flow, all the statistical properties of the flow are supposed to be spatially invariants. This assumption allows investigating the flow way further by introducing many simplifications.

According to Reynolds decomposition, a generic quantity defining the turbulent field, such as the velocity u, can be separated from its fluctuations as follows:

$$u(x,y,z,t) = \overline{u(x,y,z,t)} + u'(x,y,z,t) \tag{2.1}$$

The spatial and temporal correlation function of a random velocity field u is defined as

$$R(x,x';t,t') = \frac{\overline{u'(x,t)u'(x',t')}}{\overline{u'(x,t)u'(x,t)}} \tag{2.2}$$

It is a statistical measure that quantifies the relationship between two variables at two different positions and instants. A negative correlation is a relationship between the two velocity fluctuations whereby they have opposite directions. A correlation of 0 shows no relation between the two fluctuations instead. In the case of an homogeneous field, the correlation does not depend on the position of the measurement points, it depends on their separation $r = x' - x$ only (BAILLY and COMPTE-BELLOT 2015). Applying this to the velocity field fluctuations u' with $t = t' = t_0$ yields

$$R_{ij}(\mathbf{x},\mathbf{r},t) = \overline{u_i'(\mathbf{x},t)u_j'(\mathbf{x}+\mathbf{r},t)} = R_{ij}(\mathbf{r},t) \tag{2.3}$$

where i and j are the velocity components. Hence, the dimensionless correlation coefficient is defined as

$$-1 \leq R_{ij}(\mathbf{x},\mathbf{x}') = \frac{\overline{u_i'(\mathbf{x})u_j'(\mathbf{x}')}}{\sqrt{\overline{u_i'^2(\mathbf{x})}\;\overline{u_j'^2(\mathbf{x}')}}} \leq 1 \tag{2.4}$$

In the following sections, the indices $(1,2,3)$ represent streamwise, normal and spanwise directions. The integral length scale Λ is the spatial macro-scale of turbulence which characterises the size of the most energetic eddies. Λ_1 and Λ_3, named Taylor macro-scales, represent the streamwise and transverse length scale respectively. These parameters represent the distance within which there is a non-negligible correlation between velocity fluctuations.

$$\Lambda_1 = \int_0^\infty f(r)dr = \pi\hat{f}(0) \qquad \Lambda_3 = \int_0^\infty g(r)dr = \pi\hat{g}(0) \tag{2.5}$$

In case of anisotropic turbulence, a coefficient α is introduced

$$\alpha = \frac{\Lambda_1}{\Lambda_3} \tag{2.6}$$

which represents the ratio of length scales thus the level of the eddy stretching along the spanwise direction. (PANTON and LINEBARGER 1974). $\Lambda_1 = 2\Lambda_3$ (WILSON 1998) applies to the case of a 2D homogeneous and isotropic turbulence. Furthermore, in the case of isotropic flow, the correlation function $f(r)$ can be defined by

$$\sigma^2 f(r) = R_{11}(r, 0, 0) \tag{2.7}$$

where σ is the total variance of the field and $f(r)$ is the longitudinal correlation function. Since in this case $R_{11}(r, 0, 0) = R_{22}(0, r, 0) = R_{33}(0, 0, r)$, a similar relation can be written for lateral correlation function $g(r)$ and R_{22}. Lateral and longitudinal correlation functions are related by

$$g(r) = f(r) + \frac{r}{2}\frac{df}{dr} \tag{2.8}$$

Moreover, according to the first Karman and Howart relation (CHASSAING 2000):

$$\int_0^\infty r g(r) dr = 0 \tag{2.9}$$

This equation shows that $g(r)$, positive for short separations, will become negative for a specific r, in contrast to $f(r)$.

Many models for turbulence spectra have been developed. The ones considered in this report can be found in Table 2.1. Von Karman's model is particularly useful since different values of the parameter ν represent some of the most used turbulence models:

- $\nu = 1/2$: Liepmann's model
- $\nu = 1/3$: original Von Karman's model
- $\nu = 7/6$: Rapid Distortion Theory (RDT) which applies to non homogeneous turbulence

A last notion is considered to be useful in the aim of this report: Taylor's hypothesis of turbulence frozen convection. Under this assumption, the advection contributed by turbulent eddies themselves is small and therefore the advection of the turbulent flow passing a fixed point can be considered as entirely due to the mean flow.

	Longitudinal correlation function	Characteristic length
Gaussian model	$f(r) = exp\left(-\frac{r^2}{L^2}\right)$	$L = \frac{2\Lambda}{\sqrt{\pi}}$
Von Karman model	$f(r) = \frac{1}{2^{\nu-1}\Gamma(\nu)}\left(\frac{r}{L}\right)^{\nu} K_\nu\left(\frac{r}{L}\right)$	$L = \frac{\Gamma(\nu)}{\sqrt{\pi}\Gamma(\nu+1/2)}\Lambda$

Table 2.1: Main turbulent correlation functions; Γ is the Gamma function and K_ν the modified Bessel function of second kind of real order ν.

2.2 Turbulent boundary layer

The behaviour of the fluid near a solid boundary is of great importance in engineering problems. The concept was firstly introduced by Prandtl in 1904: he made the assumption that close to the wall the tangential length scales are greater than the wall-normal ones. On the contrary, the derivatives are much important in the wall-normal direction. These approximations set the first basis of understanding and modelling of boundary layers. This section focuses on the boundary layer formed with the impingement of a uniform velocity non-turbulent flow on a smooth flat plate.

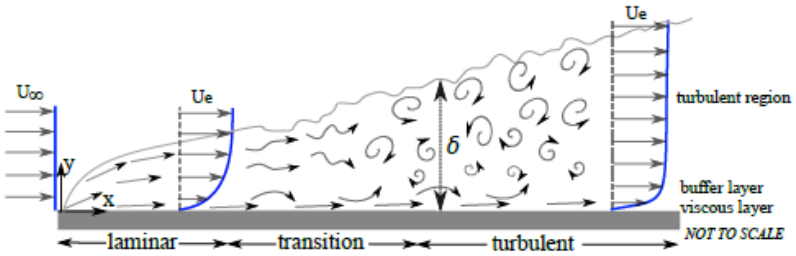

Figure 2.2: Schematic of a boundary layer transitioning from laminar to turbulent.

2.2.1 Mean flow properties and law of the wall

To predict the flow pattern, the dimensionless Reynolds number is used. It depends on the distance from the leading edge x, on the outer flow velocity U_e and on flow viscosity μ:

$$Re = \frac{\rho U_e x}{\mu} \tag{2.10}$$

Under the assumption of a large external Reynolds number, the boundary layer develops along the streamwise direction. The laminar boundary

layer close to the leading edge is formed by smooth streamlines approximately parallel to the wall. When the Reynolds number exceeds a specific value which depends on the level of flow perturbations, the transition from laminar to turbulent boundary layer occurs. Near the solid boundary, molecular diffusion is sufficient to make particles adhere to the surface as in laminar flows. However, the effect of turbulence must be considered for locations farther from the wall.

The boundary layer thickness $\delta(x)$ is commonly defined as the point where the velocity reaches 99% of the free-stream velocity. Total pressure is used instead of velocity in the case of loaded profiles since the external flow is deflected and one cannot define a constant free-stream velocity. Other integral thicknesses are the displacement and momentum thickness.

$$\delta^* = \int_0^\infty \left(1 - \frac{U}{U_e}\right) dx_2 \qquad \theta = \int_0^\infty \frac{U}{U_e}\left(1 - \frac{U}{U_e}\right) dx_2 \tag{2.11}$$

where U is the mean flow velocity at the wall distance x_2. The ratio between them is the shape factor $H = \delta^*/\theta$. It characterizes the flatness of the boundary layer mean streamwise velocity profile. Conventionally, for a laminar boundary layer over flat plate the shape factor is H = 2.59. For turbulent boundary layer with zero-pressure-gradient (ZPG), this value is around 1.3 - 1.4.

A fully developed turbulent boundary layer with zero pressure gradient on a flat plate is now considered. The no-slip condition for a viscous fluid results in a wall shear stress τ_w. In a laminar boundary layer, the gradient of velocity along the wall-normal direction produces a viscous shear stress:

$$\tau_v = \mu \frac{\partial U}{\partial x_2} \tag{2.12}$$

In a turbulent boundary layer, this quantity is dominant close to the wall. Farther from the wall, an additional term named Reynolds stress takes over, generated by flow unsteadiness.

$$\tau_t = -\rho \overline{u'v'} \tag{2.13}$$

The total shear stress is the sum of the two shear stresses. At the wall, Reynolds stresses are zero. So as to compare different boundary layer, a scaling based on friction velocity and viscosity is introduced:

$$x_2^+ = \frac{x_2 u_\tau}{\nu} \qquad U^+ = \frac{U}{u_\tau} \tag{2.14}$$

Different regions in the boundary layer can be distinguished as a function of shear stress:

- viscous sub-layer ($x_2^+ \lesssim 7$): viscous effects are predominant
- buffer layer ($7 \leq x_2^+ \leq 30$): viscous and turbulent effects are similar
- logarithmic-layer and outer-layer ($x_2^+ \gtrsim 30$): turbulent effects dominate

Three velocity scales can be defined in the wall-normal direction: $U \sim U_e$, which represents the advection by the average flow; u', which represents the turbulent diffusion and $u_\tau = \sqrt{\tau/\rho}$, the friction velocity, which characterises the near-wall region.

2.2.2 Adverse pressure gradient

In the previous section, turbulent boundary layers with a zero pressure gradient in the streamwise direction have been considered. In the real world, this condition is rare for wall bounded flows. A pressure gradient is often encountered when flows advance along curved surfaces, such as airplane wings or turbine blades. It may lead to the separation of the boundary layer. Therefore, the understanding of this phenomenon is critical.

Adverse pressure gradient (APG) corresponds to an increase of static pressure along the airfoil chord in the direction of the flow ($dP_e/dx > 0$), due to the airfoil camber or angle of attack for subsonic flows. A strong, extended APG causes the boundary layer to separate. The phenomenon is accompanied by large-scale unsteadiness and reverse flow. Euler equation for momentum conservation is now considered:

$$\frac{dP_e}{dx} = -\rho U_e \frac{dU_e}{dx} \tag{2.15}$$

Hence, adverse pressure gradient is related to decelerating flows ($dU_e/dx < 0$) while favourable pressure gradient (FPG, $dP_e/dx < 0$) to flows which tend to accelerate. Clauser's dimensionless parameter allows to quantify the pressure gradient in the streamwise direction. It represents the ratio of the pressure gradient to the wall friction.

$$\beta_c = \frac{\delta^*}{\tau_w} \frac{dP_e}{dx} \tag{2.16}$$

Eventually, the adverse pressure gradient makes the mean velocity profile flatten and the skin friction coefficient $c_f = \tau_w/(0.5\rho U_e^2)$ decrease.

2.3 Acoustic analogies

2.3.1 Acoustic propagation

The issue of trailing-edge noise at low Mach number was first examined by Powell in 1959. He used similarity arguments to estimate the strength of aerodynamic dipole sources located near the trailing-edge of a flat plate. Since then, theoretical models to predict the trailing-edge noise have been developed, based on experimental data.

According to Howe (HOWE 1978), almost all theories about acoustic propagation can be classified into three categories, depending on the aerodynamic quantity related to acoustic pressure in the far field :

a) models based on Lighthill's work, which express acoustic pressure in terms of vortical velocity components around trailing-edge. This is the case of Ffowcs Williams & Hall theory.

b) models based on the resolution of the linearised hydro-acoustic equations, such as Curle's. They relate acoustic pressure to the statistics of aerodynamic wall-pressure upstream TE.

c) ad hoc models.

The main acoustic propagation theories will be briefly summarised below.

Lighthill's theory

According to Lighthill's analogy, a propagating turbulent flow can be replaced by equivalent sources radiating in a medium at rest in the case of a far-field observer. This approach allows to compute a formally equivalent problem of linear acoustics rather than resolving unsteady and compressible equations. Navier-Stokes equations are the basis of the method. Lighthill combined the time derivative of the conservation of mass equation and the space divergence of the momentum one and introduced a reference fluid of density $\rho' = \rho - \rho_0$ and pressure $p' = p - p_0$. Thus, he obtained a wave equation:

$$\frac{\partial^2 \rho'}{\partial t^2} - c_0^2 \frac{\partial^2 \rho'}{\partial x_j^2} = \frac{\partial^2 (T_{ij})}{\partial x_i \partial x_j} \tag{2.17}$$

characterised by a quadrupole-kind source term, the double derivative of the so-called Lighthill's stress tensor T_{ij}.

$$T_{ij} = \rho u_i u_j + \left(p' - c_0^2 \rho'\right) \delta_{ij} - \tau_{ij} \tag{2.18}$$

The equation can be formally solved by Green's function technique, as far as the listener's is in the far field. This means that the distance between the source of noise and the listener are larger than the wavelength $\lambda = c_0/f$ of the source. The RHS represents the source region, with Lighthill's tensor as source term. The LHS is the propagating region: since the far-field is isentropic, this allows shifting from ρ' to p'.

Under the assumptions of large Reynolds numbers (thin boundary layer, inertial effects stronger than viscous effects) and small Mach number fluctuations ($(p' - c_0^2\rho')\,\delta_{ij} \ll \rho u_i u_j$), the stress tensor simplifies to the Reynolds stress tensor to $T_{ij} \sim \rho u_i u_j$. The observer is supposed to be in the acoustic far field.

An expansion of Lighthill's tensor allows identifying two different terms: the self noise (noise generation) and the shear noise (noise propagation). The clear advantage of Lighthill's formulation is the non-linearisation of Navier-Stokes equations. The equation takes into account not only the sound generation, but also its reflection and scattering effects. However, the resolution is not mathematically rigorous.

Ffowcs Williams & Hall's theory

Ffowcs Williams and Hall solved Lighthill's equation by a half-plane Green's function for rigid bodies in arbitrary motion in free space (HOWE 1978). The airfoil is considered as a semi-infinite half-plane with zero thickness.

Their approach consists in suppressing the volume of the body, replacing it by the fluid, and introducing sources of mass and momentum in order to force the original discontinuity represented by the body. Body motion is replaced by a continuous distribution of stationary sources. By this means, Ffowcs Williams and Hall obtained the far field mean square sound pressure $< p^2 >$ produced by a turbulent eddy as a function of vortical velocity components (HOWE 1978).

The real target of the theory is to find a proper Green's function $G(x, y, t, \tau)$ which satisfies the wave equation. In the case of free field, it is

$$\frac{1}{c^2}\frac{\partial^2 G}{\partial t^2} - \frac{\partial^2 G}{\partial x_j^2} = \delta(t-\tau)\delta(x-y) \tag{2.19}$$

in which δ is Dirac distribution. G is a function of source location y, observer location x, emission and reception time τ and t. Exact Green's functions are known for simple geometries only, obtaining a tailored function is more complicated and often requires numerical computation. Ffowcs William and Hall's theory exploits the Green function on a half-plane.

A general integral solution of (2.17) was then given by Goldstein, stating that the acoustic pressure in presence of a solid body of surface S is:

$$\begin{aligned} p'(\mathrm{x},t) = &\int_{-\infty}^{+\infty}\int_{V} \frac{\partial^2 G}{\partial y_i \partial y_j}(\mathrm{x},\mathrm{y},t-\tau)T_{ij}(\mathrm{y},\tau)\mathrm{d}^3\mathrm{y}\mathrm{d}\tau \\ &+ \int_{-\infty}^{+\infty}\oint_{S} \frac{\partial G}{\partial y_i}(\mathrm{x},\mathrm{y},t-\tau)p'_{ij}(\mathrm{y},\tau)\mathrm{d}^2\mathrm{y}\mathrm{d}\tau \\ &- \int_{-\infty}^{+\infty}\oint_{S} \frac{\partial G}{\partial \tau}(\mathrm{x},\mathrm{y},t-\tau)\rho_0 u_n(\mathrm{y},\tau)\mathrm{d}^2\mathrm{y}\mathrm{d}\tau \end{aligned} \tag{2.20}$$

According to (2.20), sound is generated by turbulent stress T_{ij} in the fluid (quadrupole source), unsteady forces exerted from the surface to the fluid $p'_{ij}n_j$ (dipole source) and from the variation of mass outflow from S (monopole source).

Curle/Amiet's theory

Curle's analogy involves compressibility effects in the source terms and it applies to the case of surfaces present in the flow. The necessary restrictions are that the surfaces bounding the flow are stationary and that the medium is at rest outside the region of turbulent flow. A free field Green's function is exploited. The pressure fluctuations are composed by three terms: the Lighthill's quadripolar integral, a monopole generated by the flux of mass through the surface and a dipole due to the instantaneous force of the surface on the fluid.

Amiet's theory is based on Curle's analogy. Its work previously covered noise production by turbulence impinging on an airfoil (AMIET 1975). The following work focused on computing the far field noise produced by turbulent flow convected past the airfoil trailing edge. It consists of a different approach with respect to Lighthill's theory and deals with non-stationary compressible flows.

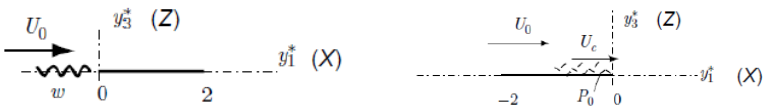

(a) (b)

Figure 2.3: LE and TE resolution sub-domains for Amiet's model.

The basis of Amiet's theory is a Helmoltz equation, obtained by temporal Fourier transform applied to a combination of the linearised Euler equations.

$$\Delta\psi + K^2\psi = 0 \quad \text{with} \tag{2.21}$$
$$\phi = \psi e^{iKMX},\ \phi' = \phi e^{i\omega t},\ X = \frac{x}{\beta},\ K = \frac{k}{\beta},\ \beta^2 = 1 - M_0^2$$

The equation is solved through the Schwarzschild technique. The boundary conditions are defined on two half planes, before and after the LE or TE depending on the application (turbulence impingement or turbulence scattering noise). The other half of the plane is considered as infinite. The imposed BC, which cancel the imaginary infinite extensions, are the following:

- LE noise: a constraint on velocity is applied by the rigidity condition on the surface. The other BC are zero potential upstream and the Kutta condition (pressure gusts must go to zero in the wake). The corresponding noise spectrum is

$$S_{pp}(\vec{x},\omega) = \left(\frac{\rho_0 k c x_3}{2S_0^2}\right)^2 \pi U_0 \frac{d}{2}\left[\varphi_{ww}\left(\frac{\omega}{U_0}, \frac{kx_2}{S_0}\right)\right]\left|\Im_{LE}\left(x_1, \frac{\omega}{U_0}, \frac{kx_2}{S_0}\right)\right|^2$$

- TE noise: a constraint on wall-pressure is imposed by Kutta condition. The other BC are zero potential upstream and the imposition of an incident pressure gust. The corresponding noise spectrum is

$$S_{pp}(\vec{x},\omega) = \left(\frac{k c x_3}{2\pi S_0^2}\right)^2 \frac{L}{2}\varphi_{pp}(\omega)\ell_z\left(\frac{kx_2}{S_0}, \omega\right)\left|\Im_{TE}\left(x_1, \frac{\omega}{U_c}, \frac{kx_2}{S_0}\right)\right|^2$$

  where φ_{pp} is the power spectral density of wall-pressure fluctuations near the TE, l_z the fluctuations transverse coherence length and the last term is an analytical radiation integral.

Trailing edge noise proves to be very small with respect to noise due to impinging turbulence on the airfoil. The validity criteria for Amiet's theory are:

$$AR \gg 1 \qquad k_x d \gg 1 \tag{2.22}$$

in which AR is the airfoil aspect ratio, k_x the chord-wise wavelength and d the semi-span. The assumptions of the theory include a frozen boundary layer at TE and a thin TE.

The main limitations to Amiet's theory are due to necessary assumptions to apply his model:

- only airfoil -like shapes are considered, with small thickness, camber and attack angle.
- upstream flow conditions are supposed to be perfectly uniform.

These conditions are rarely achieved in industrial applications, such as wind turbines or fans. This is the reason why models containing corrections of Amiet's theory drew up. For instance, (ROGER and MOREAU 2005) aim at considering the effects of a limited chord length. The article proposes a leading edge back-scattering correction and the introduction of 3D gusts to the model.

Wall-pressure fluctuations intensity and the intensity of broadband noise generated by the airfoil are strongly linked, as demonstrated by (AMIET 1976). The Power Spectral Density of far-field sound (2.23) for an observer at (x_1, x_2, x_3) and an angular frequency ω is proportional to a radiation integral $\mathcal{I}$ and to the wall-pressure wavenumber spectral density Π_0. k is the acoustic wavenumber, U_c the turbulence convection velocity and S_0 a distance accounting for the acoustic waves convection.

$$S_{pp}(\mathrm{x}, \omega) \propto \left|\mathcal{I}\left(\frac{\omega}{U_c}, k\frac{x_2}{S_0}\right)\right|^2, \Pi_0\left(\omega, k\frac{x_2}{S_0}\right) \tag{2.23}$$

The wall-pressure wavenumber spectral density is in turn proportional to the span-wise correlation length ℓ_y and to the aerodynamic wall-pressure spectrum φ_{pp} that represents the source of noise. $k_2^* = k\frac{x_2}{S_0}$ is the normalised wavenumber.

$$\Pi_0\left(\omega, k\frac{x_2}{S_0}\right) \propto \varphi_{pp}(\omega),\ \ell_y(k_2^*, \omega) \tag{2.24}$$

Pressure fluctuations at trailing-edge are a blend of turbulent fluctuations due to wall-pressure or induced by TE singularity. φ_{pp} measurements must be done near trailing-edge but far enough upstream for the information to correspond only to the incident pressure-field of boundary layer (BL) turbulence, otherwise TE scattering will affect results. Moreover, in the case of a measurement taken too far upstream, turbulence can still radically change before reaching the trailing-edge.

2.3.2 Source models

The computation of trailing-edge noise identifies the wall-pressure spectrum near TE as a source of noise within the framework of Amiet's theory. Therefore, empirical, semi-empirical and statistical models were created to represent pressure disturbances in airfoil boundary layers.

Semi-empirical models

A detailed review of all semi-empirical wall-pressure spectra has been provided by Lee (LEE 2018). Earlier models could be applied only to simplified flows, such as turbulent flows on a flat plate with zero pressure gradient. Experimental data showed that an adverse pressure gradient has a significant impact on wall-pressure spectrum. The understanding of this condition is then crucial to analyse the phenomenon of boundary layer separation. For this reason, recent studies starting from Rozenberg's focused on extensions of previous models to account for adverse pressure gradient effects. ZPG is kept as a reference for the lowest pressure fluctuations. Wall-pressure spectra models differ from the parameters used to scale experimental data of similar flow conditions so as to make them collapse. A brief description of main semi-empirical models will follow.

- *Corcos model*

  This is one of the first attempts to create a wall-pressure spectrum model for a fully turbulent boundary layer over a flat plate with zero pressure gradient. The correlation length of turbulence is stated to be inversely proportional to frequency.

  $$\ell_y(k_2^*, \omega) = \frac{\omega/(b_c U_c)}{k_2^2 + \omega^2/(b_c U_c)^2} \tag{2.25}$$

  where b_c is a constant and U_c turbulence convection velocity. Even if this formulation is still largely used, the model consistency at low frequencies has been questioned and many corrections proposed to correct its overestimations. However, the model proved reliable for medium-high frequencies if turbulence is almost homogeneous. It is mainly used for short-term acoustic calculations (ROGER and MOREAU 2005).

- *Goody's model*

  This model draws inspiration from Chase - Howe's spectral model:

  $$\frac{\varphi(\omega) U_e}{\tau_w^2 \delta^*} = \frac{2(\omega\delta^*/U_e)^2}{[(\omega\delta^*/U_e)^2 + 0.0144]^{3/2}} \tag{2.26}$$

  where δ^* is the displacement thickness. The model spectrum proposed in (2.26) is proportional to ω^2 at low frequencies and to ω^{-1} at higher

frequencies. However, Goody remarks the lack of a consistent spectral decay at the highest frequencies ($\omega \to \infty$). His model accounts for the effects of Reynolds number through three coefficients ($C_1,\ C_2,\ C_3$) so as to better agree with experimental data. The resulting wall-pressure spectrum as a function of frequency ω is

$$\frac{\varphi(\omega)U_e}{\tau_w^2\delta} = \frac{C_2(\omega\delta/U_e)^2}{[(\omega\delta/U_e)^{0.75} + C_1]^{3.7} + [C_3(\omega\delta/U_e)]^7} \tag{2.27}$$

in which U_e is the velocity at boundary-layer edge, τ_w the shear stress at wall and δ the boundary-layer thickness. Previous models have been modified in order to represent a spectrum increase proportional to ω^2 at low frequencies, a decay as $\omega^{0.7}$ in the mid-range and a strong decay as ω^{-5} at the highest frequencies. The uncertainty with regard to experimental data decrease to $\pm 4\ dB$ in this case (GOODY 2004). Goody introduces different parameters to scale data depending on the frequency range. At low frequencies, outer-layer parameters are exploited to make spectra collapse, whereas in the high range inner-layer scales are used.

- *Rozenberg's model*

  Since in many applications the turbulent boundary layer upstream of the trailing edge is subject to an adverse mean-pressure gradient, this model is the first to account for its effects on pressure fluctuations statistics. Previous studies pointed out an increase of 10 dB in the low frequencies range in case of adverse pressure. If the effect is not taken into account, the models lead to a significant underestimation of trailing-edge noise. While resolving the underestimations at low frequencies, Rosenberg model still proves unreliable at the highest ones. As a matter of facts, its rapid transition from the mid-region to the high frequency one does not follow the experimental data trend. This model consists of a Goody's model update by slightly changing the scaling approach. Local parameters are used, so as to take into account boundary-layer history (ROZENBERG et al. 2012):

  - displacement thickness δ^* is used instead of boundary layer thickness δ.
  - the maximum shear stress τ_{max} is used to scale wall-pressure fluctuations.
  - in the mid-frequencies region (overlap region) the spectrum can decay more than $\omega^{0.7}$.
  - if the pressure gradient parameters increase, such as Clauser parameter, the global level of fluctuations increase.

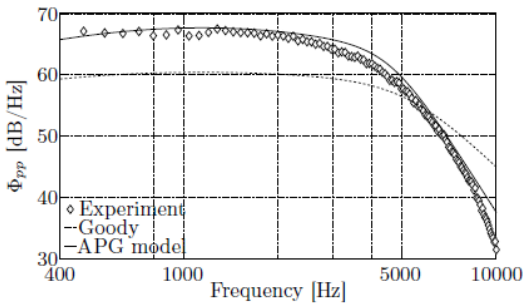

Figure 2.4: Comparison of wall-pressure fluctuations spectra for Goody's and Rozenberg's models (V2 airfoil RMP23), see (ROZENBERG et al. 2012).

- *Hu and Herr's model*

  This model accounts for both adverse and favourable pressure gradient flows. It takes Goody's model as starting point and introduces a new parameter $H = \delta^*/\theta$ (in which θ is the boundary-layer momentum thickness) as it has a direct correlation with boundary-layer velocity profile and then with pressure gradient (HU and HERR 2016). Hu and Herr are the first to consider the effect of a non-frozen turbulence, in which the Taylor hypothesis of equivalence between time and spatial scales cannot be applied. Moreover, they analysed the weight of the turbulence-turbulence interaction term in Poisson equation (2.28) which will be addressed later on.

Eventually, Lee provided an empirical model summarizing all previous ones, valid over a large range of frequencies and flow conditions (LEE 2018).

Statistical models

Another way to express wall-pressure Power Spectral Density (PSD) is to use statistical models, such as Kraichnan's (KRAICHNAN 1956). It is based on the solution of Poisson equation (2.28), either in space or in frequency domain. Poisson equation derives from Reynolds decomposition of the incompressible moment equation: the velocity field u_i is split in a sum of a steady component $\overline{U}_i$ and fluctuations from average u_i'.

$$\frac{1}{\rho}\nabla^2 p = \underbrace{-2\frac{\partial u_j}{\partial x_i}\frac{\partial U_i}{\partial x_j}}_{1} \underbrace{- \frac{\partial^2}{\partial x_i \partial x_j}(u_i u_j - \overline{u_i u_j})}_{2} \tag{2.28}$$

The indices i and j represent streamwise (1), normal-to-wall (2) and transverse (3) directions. The sources generating pressure fluctuations are split in two terms (see (2.28)):

1. the interaction between turbulence and mean shear.

2. the non-linear interaction between turbulent fluctuations components.

Under the assumption of homogeneous turbulence in planes parallel to the wall, (2.28) can be Fourier-transformed in space along (x_1, x_3) directions.

$$\frac{\partial^2 \hat{p}\left(\boldsymbol{k}, x_2\right)}{\partial x_2^2} - k^2 \hat{p}\left(\boldsymbol{k}, x_2\right) = -2\rho \mathrm{i} k_i \frac{\partial U_i}{\partial x_j} \hat{u}_j\left(\boldsymbol{k}, x_2\right) \tag{2.29}$$

By solving the obtained Helmholtz equation to get to $\hat{p}(\boldsymbol{k}, x_2 = 0)$, the PSD of wall-pressure fluctuations can be computed. The contribution of the turbulence - mean shear interaction is the only one considered as significant in the derivation of $\varphi_{pp}(\boldsymbol{k})$ (2.32).

$$\begin{aligned} \varphi_{pp}^{TM}(\boldsymbol{k}) = 4\rho_0^2 \int_{\boldsymbol{k}'} \int_0^{\infty} \frac{k_1^2}{k^2} \mathrm{e}^{-\left(X_2 + X_2'\right)k} \frac{\partial U_1\left(X_2\right)}{\partial x_2} \frac{\partial U_1\left(X_2'\right)}{\partial x_2} \\ \left\langle \hat{u}_2\left(\boldsymbol{k}, X_2\right) \cdot \hat{u}_2\left(\boldsymbol{k}', X_2'\right) \right\rangle \mathrm{d}X_2 \mathrm{d}X_2' \mathrm{d}\boldsymbol{k}' \end{aligned} \tag{2.30}$$

The normal-to-wall velocity fluctuations statistics are modelled through the normalised cross-spectrum of u_2, S_{22}:

$$\left\langle \hat{u}_2\left(\boldsymbol{k}, X_2\right) \cdot \hat{u}_2\left(\boldsymbol{k}', X_2'\right) \right\rangle = S_{22}\left(\boldsymbol{k}, X_2, X_2'\right) \delta\left(\boldsymbol{k} - \boldsymbol{k}'\right) \tag{2.31}$$

$$\varphi_{pp}^{TM}(\boldsymbol{k}) = 4\rho_0^2 \int_0^{\infty} \frac{k_1^2}{k^2} \mathrm{e}^{-\left(X_2 + X_2'\right)k} \frac{\partial U_1\left(X_2\right)}{\partial x_2} \frac{\partial U_1\left(X_2'\right)}{\partial x_2} S_{22} \mathrm{d}X_2 \mathrm{d}X_2' \tag{2.32}$$

Under the assumption of frozen turbulence, the streamwise number spectrum is transformed into a frequency spectrum through scaling with the convection velocity U_c:

$$\varphi_{pp}(\omega) = \frac{\int_{-\infty}^{+\infty} \varphi_{pp}^{TM}\left(K_c, k_3\right) \mathrm{d}k_3}{U_c} \tag{2.33}$$

The wavenumber spectrum of pressure fluctuations depends on an exponential decay, on the mean velocity gradient and on the root-mean-square of vertical velocity. The last term of (2.32), S_{22}, depends on the choice of the turbulence spectrum (Table 2.1). It is the real part of the double spatial Fourier transform of the vertical velocity two-point correlation R_{22} in the streamwise and transverse directions.

The following analytical models are considered in this report:

- Gaussian energy spectrum, one of the simplest models in literature:

$$S_{22}\left(\boldsymbol{k}, x_2, x_2'\right) = \frac{\sqrt{\overline{u_2^2}\left(x_2\right)\overline{u_2^2}\left(x_2'\right)}L^4}{16\pi} k^2 \exp\left(-\frac{L^2k^2}{4} - \frac{\left(x_2 - x_2'\right)^2}{L^2}\right) \tag{2.34}$$

- Generalised Von Karman energy spectrum

$$\begin{aligned} S_{22}\left(\boldsymbol{k}, x_2, x_2'\right) &= \frac{\sqrt{\overline{u_2^2}\left(x_2\right)\overline{u_2^2}\left(x_2'\right)}l^2\tilde{k}^2\zeta^{\nu+2}}{\Gamma(\nu)\pi 2^{\nu+1}\left(1+\tilde{k}^2\right)^{\nu+2}} K_{\nu+2}(\zeta) \\ \zeta &= \frac{\|x_2 - x_2'\|}{l}\sqrt{1+l^2k^2} \end{aligned} \tag{2.35}$$

In the case of $x_2 \to x_2'$, the auto-spectrum is obtained:

$$S_{22}^a\left(k, x_2\right) = \frac{\nu(\nu+1)\overline{u_2^2}\left(x_2\right)l^4k^2}{\pi\left(1+l^2k^2\right)^{\nu+2}} \tag{2.36}$$

Different values of ν correspond to the models listed in section 2.1.

2.4 Numerical methods

Computational Aero-Acoustics (CAA) is a relatively new branch of aero-acoustics which deals with the generation of noise by turbulent flows through numerical methods. Two kinds of these methods can be identified, namely hybrid methods and direct methods. Moreover, LBM (Lattice Boltzmann Method) has recently provided interesting results in trailing-edge noise applications, compared to traditional Navier Stokes solvers.

2.4.1 Hybrid methods

Computation of flow and sound are decoupled. These methods generally comprise two or three stages: the noise generation and near-field propagation (turbulent flow), the mid-field propagation (steady flow) and the far-field propagation (steady and homogeneous flow). This kind of simulation allows using incompressible equations in case of low Mach numbers and resolving flow in a small area around the source only.

An example of hybrid method is the solver sAbrinA developed by ONERA (MINCU and MANOHA 2014). So as to predict the aircraft engine acoustic installation, the computational steps are the following:

1. The noise generation and near-field propagation are computed by a CAA solver up to a control surface.

2. The acoustic field on the control surface is then exploited to derive the incident acoustic field on the aircraft scattering surface and at a specific observer position by a Kirchhoff method.

3. The scattered acoustic field is computed by solving a Helmholtz equation. The total acoustic field will be the sum of all the computed acoustic contributions.

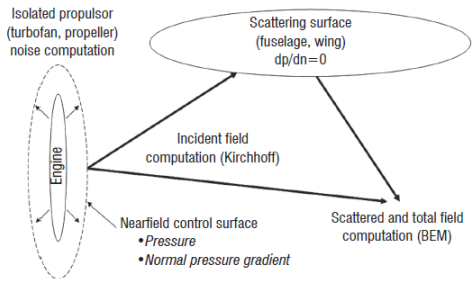

Figure 2.5: Computational strategy of ONERA hybrid method for the prediction of installation effects (MINCU and MANOHA 2014).

2.4.2 Direct methods

Direct methods aim at the computation of flow field and sound at the same time. Cases in point are LES (Large Eddy Simulation), URANS (Unsteady Reynolds-Averaged Navier Stokes) and DNS (Direct Numerical Simulation) that will be detailed later. Characterised by high computational cost due to the acoustic field extent, all these methods require a high number of time steps for stability reasons.

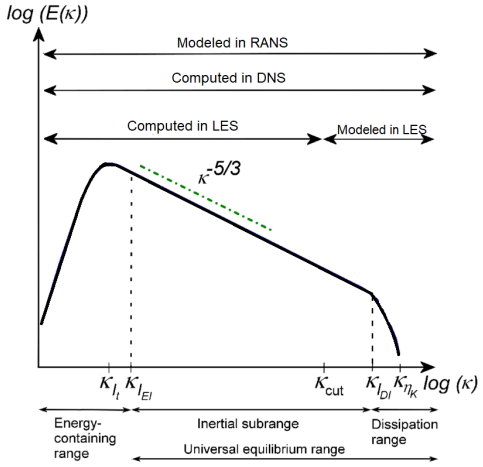

Figure 2.6: Fields of application of different direct numerical techniques so as to resolve the turbulent energy spectrum as a function of wavenumber. Reynolds-Averaged Navier Stokes equations appear to be the less expensive method, since totally based on turbulence modelling and time-averaging. On the other hand, Large Eddy Simulations compute flow up to a cutting frequency. The most expensive method is Direct Numerical Simulation, which resolves all scales of motion.

DNS aims at resolving the whole range of spatial and temporal scales of the turbulence while computing compressible Navier-Stokes equations (2.37).

$$\begin{aligned} \frac{\partial \rho}{\partial t} + \frac{\partial (\rho u_k)}{\partial x_k} &= 0 \\ \frac{\partial (\rho u_i)}{\partial t} + \frac{\partial (\rho u_i u_k + p\delta_{ik} - \tau_{ik})}{\partial x_k} &= 0 \\ \frac{\partial (\rho E)}{\partial t} + \frac{\partial \left[\rho u_k \left(E + p/\rho \right) - u_i \tau_{ik} + q_k \right]}{\partial x_k} &= 0 \end{aligned} \tag{2.37}$$

Since DNS relies does not rely on any turbulence model, in contrast to RANS and LES approaches, this method requires the highest computation cost and memory storage even at low Reynolds numbers. Nevertheless, its spatial resolution makes DNS a useful tool for research, while RANS approach remains

the most common industrial tool in the prediction of compressible flow fields.

An approximation of the covered scale is given by:

$$\frac{L_f}{l_\eta} \sim Re_{L_f}^{3/4} \tag{2.38}$$

in which L_f is the integral scale turbulence, giving an order of magnitude of vortices dimensions, and l_η is the so-called Kolmogorov scale, the smallest vortex dimension of the flow. Re_{L_f} is the Reynolds number of the flow, computed through fluctuations velocity and the integral scale as $Re_{L_f} = (u' L_f)/\nu$ (BAILLY and COMPTE-BELLOT 2015). The mesh points number is given by:

$$N \propto Re_{L_f}^{9/4} \tag{2.39}$$

These orders of magnitude make us understand the computational weight of DNS and the impossibility to apply it to engineering case studies for the time being. However, it is used for turbulent model validation, compared to experimental data.

Numerical considerations of DNS

Numerical schemes

The aforementioned Navier-Stokes equations are solved through a discretisation in space and in time. The majority of structured-mesh based DNS solvers exploit the spatial finite differences discretisation thanks to the easiness of high order schemes development. The key concept of finite difference is the search for an approximate solution of a partial differential set of equations at the grid points. The derivatives are approximated by linear combinations of function values on the mesh. The mesh can be cartesian or formulated with generic curvilinear coordinates by a change of variables. The domain is discretised in a certain number of points, in space and time.

The spatial derivatives in proximity to a mesh point

$$\frac{\partial u}{\partial x}(x) = \lim_{\Delta x \to 0} \frac{u(x + \Delta x) - u(x)}{\Delta x} \tag{2.40}$$

are approximated by a Taylor's expansion

$$u(x + \Delta x) = u(x) + \Delta x \frac{\partial u}{\partial x}(x) + \frac{\Delta x^2}{2} \frac{\partial^2 u}{\partial x^2}(x) + \cdots \tag{2.41}$$

so as to obtain

$$\frac{u(x + \Delta x) - u(x)}{\Delta x} = \frac{\partial u}{\partial x}(x) + \mathcal{O}(\Delta x) \tag{2.42}$$

where $\mathcal{O}(\Delta x)$ represents the truncation error. This latter shows the order of accuracy of the scheme and depends on the number of points involved in the stencil around the considered point.

Another spatial discretisation method useful in the framework of this work is the spectral one. It consists of the discretisation of the Fourier transforms of Navier-Stokes equations and it is suited to periodic problems. A periodic function can be expressed though a Fourier series as

$$f\left(x_i\right) = \sum_{q=-N/2}^{(N/2)-1} F\left(k_q\right) \exp^{\mathrm{i}k_q x_i} \tag{2.43}$$

where $x_i = \mathrm{i}\Delta x$ and $k_q = 2\pi q/\Delta x N$. This expression is used to interpolate a continuous function $f(x)$. Spectral methods can be defined as global: high order polynomials are exploited and their great accuracy allows a less refined mesh than in the finite differences application. The main idea is to write the solution of the differential equation as a sum of certain basis functions and then to choose the coefficients of the sum so as to satisfy the differential equation as well as possible.

As far as temporal discretisation, finite differences method will be considered. A Taylor development in time is applied:

$$u(x,t+k) = u(x,t) + k\frac{\partial u}{\partial t}(x,t) + \frac{k^2}{2!}\frac{\partial^2 u}{\partial t^2}(x,t) + \cdots + \frac{k^n}{n!}\frac{\partial^n u}{\partial t^n}(x,t) \tag{2.44}$$

At the n order:

$$u(x,t+k) = \exp\left(k\frac{\partial}{\partial t}\right) u(x,t) \tag{2.45}$$

Temporal discretisation can be carried out in two ways. An explicit scheme allows to compute solution at the instant t^{n+1} on a grid point x_j through the solution at previous instants t^{n-1}, t^{n-2}. It basically calculates the state of the system at a later time from the state of the system at the current time. On the contrary, implicit methods find a solution by solving an equation involving both the current state t^n of the system and the later one t^{n+1}. DNS solvers usually employ high order Runge-Kutta methods, renowned for their accuracy and stability. The error introduced by a temporal scheme is the dissipation effect, which applies a damping to the solution. Dissipation effects are assessed by studying the ratio u_i^{n+1}/u_i^n.

Boundary conditions

Imposing the right boundary conditions is one of the main issues of numerical simulation, especially as far as computational aeroacoustics is concerned. Acoustics need to radiate outside the domain without spurious noise and vortical waves must be convected and damped. The main categories of boundary conditions (BC) are:

- characteristic BC: they deal with small perturbations, locally one dimensional and inviscid. The waves are classified depending on their propagation direction. If the wave is outcoming: it is computed using an upwind scheme, if it is incoming: it is computed following the type of the boundary condition. This kind of boundary condition can be easily applied to any kind of boundary (inlet, outlet, interface...). Anyway, since the method is locally 1D, this represents an issue when dealing with discontinuities

- sponge zones: they consist of highly diffusive zones, where fluctuations are removed through imposing high viscosity. The windowing function allows a smooth transition and avoid spurious noise generation. This method is used in the case of disturbances of large amplitude.

- perfectly match layers: an extra domain is created where waves are damped as in an anechoic chamber, absorbed by the additional layers. This kind of BC applies to any type of wave of boundary. However, the extra layers are difficult to be handled with a parallel code.

2.4.3 Lattice - Boltzmann Method

LBM simulations have provided some interesting results for trailing-edge noise analysis. Compared to classical CFD tools based on the discretisation of Navier-Stokes equations, LBM is promising as far as integration time and scalability since the equation system resolution proves simpler. The method was developed at the end of the nineties and since then it has been exploited in aeroacoustics more and more. LBM simulation is a mesoscopic technique, based on gas kinetic theory. It considers a probability distribution of particles $f(\mathbf{x},\mathbf{c},\mathrm{t})$ characterised by a velocity $\mathbf{c}$ at the position $\mathbf{x}$ at instant t. The time and space evolutions of this probability function are tracked on a lattice grid when the particles are subjected to an external force. The Lattice - Boltzmann advection equation is:

$$f_i(x^* + c_i^* \Delta t^*, t^* + \Delta t^*) - f_i(x^*, t) = C_i(x^*, t^*) \tag{2.46}$$

in which C_i is the so-called collision factor, accounting for the effect of particles collisions which are considered to be binary and elastic. At equilibrium,

the collision operator is null and f follows a Maxwell-Boltzmann distribution. The method is particularly handy since the moments of f over the considered volume (composed by cells named *voxels*) are:

1. $\rho = \int_{\mathbb{R}^3} f d\mathbf{c}$
2. $\rho\mathbf{u} = \int_{\mathbb{R}^3} f\mathbf{c} d\mathbf{c}$
3. $\rho\left(e + \frac{1}{2}u^2\right) = \int_{\mathbb{R}^3} f|\mathbf{c}|^2 d\mathbf{c}$

Through them, a macroscopic description of the Navier-Stokes equations can be obtained.

A model named BGK (Bhatnagar, Gross and Krook) has been proposed to simplify the collision operator as:

$$\left(\frac{\partial f}{\partial t}\right)_{collision} = -\frac{1}{\tau}(f - f^{eq}) \tag{2.47}$$

where τ is the collision relaxation time. The final equation writes

$$\frac{\partial f}{\partial t} + c_i\frac{\partial f}{\partial x_i} + \frac{F_i}{m}\frac{\partial f}{\partial c_i} = -\frac{1}{\tau}(f - f^{eq}) \tag{2.48}$$

f is then developed through Hermite polynomials: the coefficients of the development will be the moments of the function. Since it is obviously impossible to solve equation (2.48) for an infinite number of particle velocities, a simplification must be chosen before computing. A common discretisation considers 19 directions for velocity on any 3D voxel, the so-called "D3Q19". It renders a perfect gas flow at low Mach number. A quadrature method is eventually used to integrate the function along the characteristic lines. In the acronym, "D" stands for the truncation order of the Hermite polynomials (only 3 elements of the expansion are considered) while "Q" refers to the quadrature method.

One of the advantages of LBM is its intrinsic compressibility that makes it really useful for TE noise applications. It can be used both in LES and DNS depending on the Reynolds number range.

3

Numerical simulation of CD airfoil at 8° AoA

The airfoil geometry considered in this internship is the Controlled Diffusion airfoil (CD) designed by Valeo. This shape is found at the mid-span region of the fan blade. The controlled-diffusion airfoils refer to a kind of cambered airfoil conceived so as to carefully control flow and losses close to the airfoil surface. It is designed analytically to be shock-free at transonic Mach numbers and to avoid boundary layer separation on the suction side for a range of inlet conditions necessary for a compressor. (HOBBS et al. 1984)

Characterised by a 4% thickness to chord ratio and a camber angle of 12°, this profile has been used for turbo-engine compressor and fan blades and automotive engine cooling fan systems. It proved in cascade testing higher critical Mach numbers, higher incidence range, and higher loading capability than standard series of airfoils designed for equivalent requirements. The CD profile shape tend to have thicker leading and trailing edges than their standard series counterparts, which lead to improved compressor durability.

The CD airfoil has been the object of experimental and numerical researches in aerodynamics and aeroacoustics over two decades. The study started from the comparison of experimental steady wall-pressure measurements and RANS simulation results attempting to reproduce the same blade loading.

3.1 Numerical set-up

Two types of numerical simulations will be analysed for the same CD airfoil: a DNS conducted using a Navier-Stokes solver (NS-DNS) and a DNS simulation using LBM (LBM-DNS). Both have been performed at a geometrical angle of attack (AoA) of $\alpha = 8°$, which is the designed working condition of this airfoil.

3.1.1 NS-DNS set-up

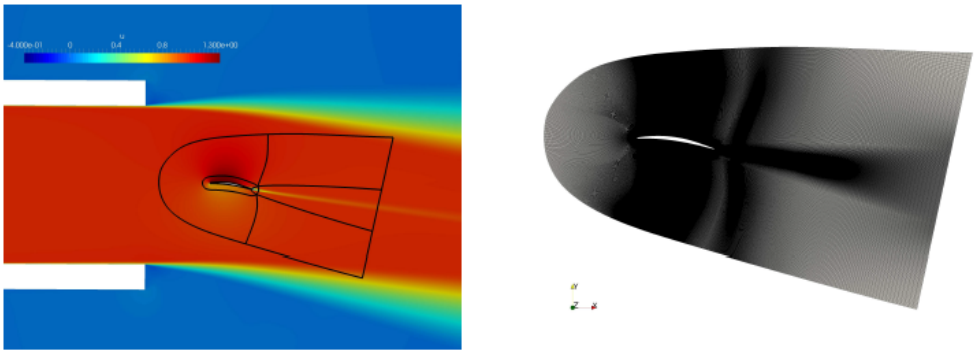

Figure 3.1: Wind-tunnel setup for RANS and DNS computations (left) and the grid in the truncated domain around the airfoil (right).

Data exploited for post-processing have been obtained by a 2D incompressible RANS computation followed by a 3D DNS (WU 2019). Previous RANS using $k - \omega$ SST model have been performed with Ansys Fluent. It has been used to infer the inlet velocity profiles, which account for the mean installation effects on the full wind tunnel set-up, and the initial field of the DNS. The flow condition is fixed at $\alpha = 8°$ and $U_0 = 16\ m/s$, with a 50 cm jet-width. The simulation had to be performed at a Mach number higher than the corresponding experimental conditions ($M = 0.25$ instead of 0.05) due to computational cost and time for such a resolution. The considered Reynolds number of $Re_c = 150000$ was the state-of-the-art for DNS simulation for trailing-edge noise studies when the simulations were run.

For DNS, the multi-block structured compressible Navier-Stokes solver HiPSTAR was used, conceived at the University of Southampton by R.D. Sandberg. 7 flow-through times were recorded at a sampling frequency of 78 kHz. The computational domain comprises six blocks. The aerofoil is surrounded by an O-type grid due to the round leading and trailing edges. The total grid size is 345 million points. The O-grid around the boundary layer comprises 3341x279x194 grid points. As far as discretisation, the following choices were adopted:

- in space: 4^{th} order central standard-difference scheme in streamwise and crosswise directions with Carpenter boundary stencils. Spectral method in spanwise direction: 96 Fourier modes with 100% dealiasing (194 collocation points in the physical space).
- in time: 4^{th} order Runge-Kutta scheme with a constant time step of $\Delta t = 7.5\ \mu s$ (CFL = 2.5). It has been chosen for the ultra low memory storage required.

Boundary conditions were set so as to avoid unphysical numerical reflections and damp the disturbances due to convected turbulence. Characteristic based boundary conditions have been used on domain boundaries and sub-domain interfaces. An adiabatic, no-slip condition is applied on the surface of the airfoil.

For post-processing, a parallel tool named FAT (Flow Analysis Tool) was exploited. The software allows to read the volumes of the primitive flow field and record them as a Plot3D format. Moreover, a Python based tool named ANTARES by CERFACS was used.

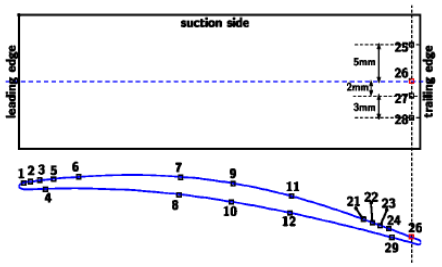

Figure 3.2: Remote microphone probes positions on the CD experimental mock-up.

The experimental data used for comparison have been obtained in the anechoic open-jet wind tunnel at Université de Sherbrooke. The CD airfoil is instrumented with Remote Microphone Probes (RMP) on the suction side along the streamwise and spanwise direction as in Figure 3.2. This internship work focuses on data from sensors 21, 22 and 24 on the suction side of the airfoil.

3.1.2 LBM-DNS set-up

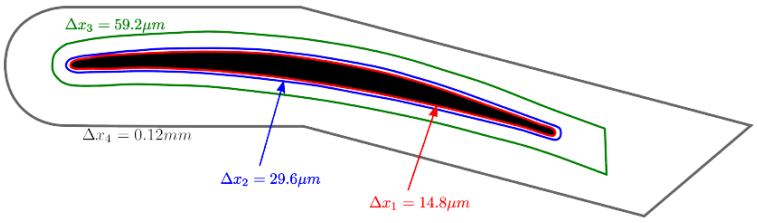

Figure 3.3: Position of the refinement volumes in the vicinity of the airfoil (SANJOSE and MOREAU 2011).

A Lattice-Boltzmann Method solver (PowerFLOW) has been used to obtain data for the present analysis. It has been successfully applied to aeroacoustics problems at similar Reynolds number. PowerFLOW directly resolves the aerodynamic and acoustic fields around the airfoil. The computational domain includes the jet nozzle geometry to correctly capture the flow in the potential core. Sponge layers have been used to damp all waves and avoid spurious reflections on the outlet boundary. The simulation includes only the mid-span section of the experimental mock-up in order to reduce the computational cost. The depth of the computational domain (about 10% of the airfoil chord) is larger than twice the spanwise coherence length measured on the wall-pressure statistics on the airfoil. Periodic boundary conditions have been applied in the spanwise direction.

The Reynolds number, the angle of attack and the inlet velocity are the same as in the DNS case. The solver set the acoustic CFL number to an unitary value. Hence, the time step is 0.11 μs. The simulation has been run for 17 flow-through times. Statistics have been recorded over the last 11 flow-through times. A DNS resolution has been achieved in the airfoil vicinity with surface resolution leading to a $\Delta y^+ \sim 1$ all along the profile surface. Even if the experimental Mach number is about 0.05, in the simulation it has been increased up to 0.2 so as to obtain a proper DNS resolution in the first 3 refinement volumes (VR). The bounds of the VR closest to the surface are shown in Figure 3.3. Their thickness is based on the experimental boundary layer profile on the suction side near the trailing-edge, where the boundary layer is the thickest on the profile. The first VR height corresponds to the viscous sub-layer of the experimental boundary profile, the second VR height corresponds to the log-law part and the last covers the wake region and extends up the non-viscous zone. The 3D mesh has 640 million voxels. In this internship work, the considered volume corresponds to DNS sensor 22.

In order to prevent numerical instabilities, the relaxation time is kept above a critical value in PowerFlow, increasing artificially the fluid viscosity. The velocity is increased by a factor 4 by the viscosity raise during the computation of the dimensionless lattice values. The speed of sound and the Reynolds number are kept constant. With a higher Mach number, the real viscosity is achieved in the first three refinement volumes, while it is lower in volumes further away with a lower mesh resolution.

3.2 NS-DNS hydrodynamic field

3.2.1 Grid resolution

The quality of a DNS depends on the grid resolution: it must be small enough to resolve the dissipative scales of turbulence. For wall bounded flows, the requirements are higher for Δy^+, since the stronger gradients are in the normal-to-wall direction. The plots depicted in Figure 3.4 show the evolution of the grid refinement in the three dimensions. They are comparable to reference DNS run with the same solver. (SANDBERG et al. 2008)

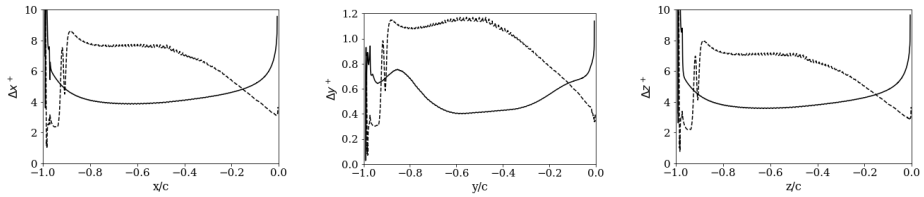

(a) (b) (c)

Figure 3.4: DNS grid resolution (solid line: pressure side, dashed line: suction side).

A further check of the correct resolution of all scales of turbulence is done through investigating the kinetic energy balance in the wall-normal direction. Turbulence kinetic energy is a very important quantity for turbulence modeling and its budget in its transport equation can provide insight into the flow physics. In the boundary-layer approximation, the equation for the turbulent kinetic energy is:

$$\begin{aligned} 0 = &-\left(< U > \frac{\partial k}{\partial x} + < V > \frac{\partial k}{\partial y} \right) + P - \tilde{\varepsilon} + \\ &+ \nu \frac{\partial^2 k}{\partial y^2} - \frac{\partial}{\partial y} < \frac{1}{2} v \mathbf{u} \cdot \mathbf{u} > - \frac{1}{\rho} \frac{\partial}{\partial y} < v p' > \end{aligned} \tag{3.1}$$

The terms in this balance equation are respectively (POPE 2000):

1. mean-flow convection
2. production
3. pseudo-dissipation
4. viscous diffusion

5. turbulent convection

6. pressure transport

For locations far from the wall, the contribution of the turbulence production term and dissipation term become dominant. The energy budgets terms are normalized by a density weighted factor of $Re_0\rho^2u^4/T$, where T is the temperature of the flow. A balance value of almost zero for all the locations along the chord proves that the DNS managed to properly resolve the dissipation range. In Figure 3.5, the budgets have been plotted for both sensor 21 and 22.

In Figure 3.5 (a), the large hump connected by two peaks of the production term curve indicates the presence of the adverse pressure gradient (WU et al. 2019). According to literature, the diffusion rate is higher for APG and negative diffusion is found below the peak of turbulent production (KROGSTAD and SKARE 1995). In (b), a comparison is made between the production and dissipation terms for sensor 21 and 22. Increased levels of both terms can be seen for the sensor nearer to the trailing edge and then subject to a stronger pressure gradient. The turbulent mixing dynamics is strongly linked to these two factors: the stronger the APG, the more enhanced the level of turbulent mixing.

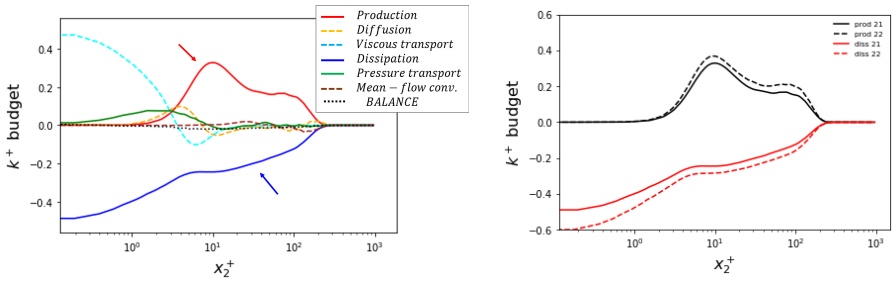

(a) (b)

Figure 3.5: Energy kinetic budget for sensor 21 (a) and comparison between the production and dissipation terms for sensor 21 and 22 (b).

3.2.2 Mean flow field

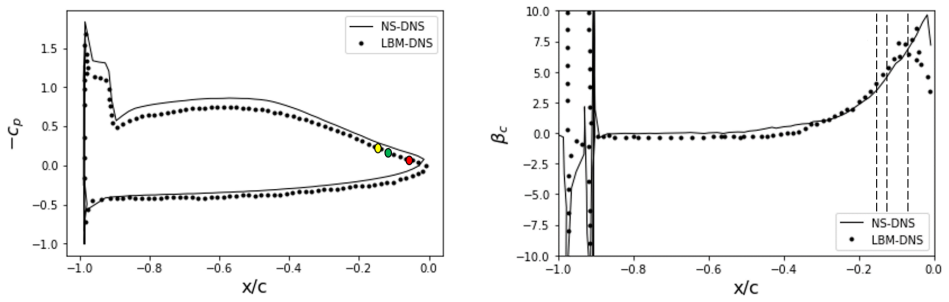

(a) (b)

Figure 3.6: (a) Pressure coefficient and (b) Clauser's parameter evolution along the CD airfoil chord for the two DNS. The dashed lines show the location of sensors 21, 22 and 24.

The pressure distribution along the airfoil is displayed through the mean pressure coefficient c_p in Figure 3.6 (a):

$$c_p = \frac{\overline{p} - p_{ref}}{1/2\rho_{ref}u_{ref}^2} \tag{3.2}$$

where p_{ref}, ρ_{ref} and u_{ref} are the reference pressure, density and velocity. As shown in the plot by the small plateau between $x/c = -1$ and $x/c = -0.8$, the transition to turbulence is triggered by a laminar recirculation bubble near the leading edge. The flow remains attached over most of the chord length. Clauser's parameter is used in Figure 3.6 (b) to show the increase of the pressure gradient along the chord (see (2.16)). The airfoil is subject to a strong and increasing adverse pressure gradient from the mid-chord to the trailing-edge as shown by the negative slope on the pressure coefficient plot.

3.3 NS-DNS Boundary layer characterisation

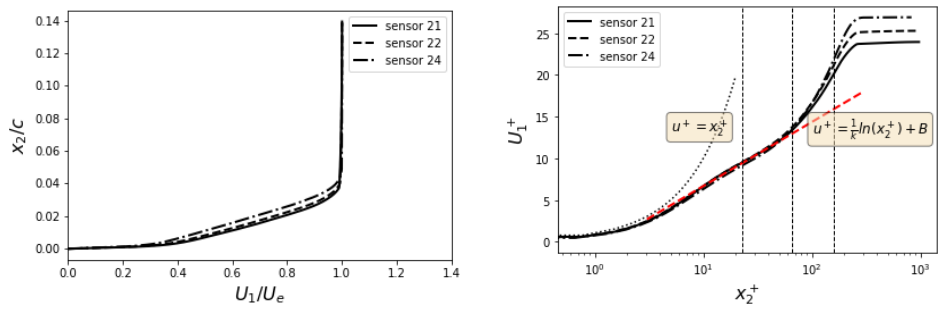

(a) (b)

Figure 3.7: (a) Tangential velocity profile. (b) Mean tangential velocity profile scaled on inner variables.

The mean velocity profiles in the wall-normal direction are presented in Figure 3.7. The adverse pressure gradient yields a flow deceleration along the profile, as shown in Figure 3.7 (a) by the difference between the two curves. The velocity profile scaled on inner variables is depicted in Figure 3.7 (b). The vertical dashed lines represent the locations chosen for further analysis in the following section. They are located in the log-layer and in the outer layer respectively. As previously mentioned, several regions can be identified in the boundary layer:

- *viscous sub-layer*, in this case for $x_2^+ \leq 5$. The profile follows a dimensionless linear low: $U^+ = x_2^+$.
- *buffer layer*, small transition zone between the viscous and the log-layer.
- *log-layer*: in this region the dynamic properties of the flow are independent of the molecular viscosity (CHASSAING 2000). The log-law, $U^+ = \frac{1}{k} \ln x_2^+ + B$ fits only a small fraction of the boundary layer ($20 \leq x_2^+ \leq 50$). The typical ZPG von Karman constant $k = 0.41$ does not fit properly the curve. A smaller value $k = 0.3$ must be considered in this case due to the effect of the pressure gradient. The constant B in this case is negative ($B = -1$). Due to the adverse pressure gradient, the normalised velocity profile lies below the standard log-law, thus indicating a reduction in the thickness of this layer. An additional way to observe the small extent of the log-layer in the considered APG case can be seen in Figure 3.8: the two peaks of $x_2^+ \partial U_1^+ / \partial x_2^+$ correspond to the logarithmic and to the outer part of the boundary layer.

- *outer layer*, for $x_2 \geq 50$, where the effect of APG can be appreciated the most: there is a consistent increase of the mean velocity relative to u_τ. The APG makes the boundary layer exhibit a more prominent wake region. The increase of Clauser parameter while approaching the TE can be properly observed for $x_2^+ > 100$, but it is also noticeable all the way down to the log-layer.

	sensor 21	sensor 22	sensor 24
δ_{p99} [mm]	4.66	4.94	5.41
H	1.86	1.89	1.94
U_e [m/s]	17.6	17.4	17.3

Table 3.1: Boundary layer integral parameters for the three sensors.

The integral parameters which characterise the boundary layer are listed in Table 3.1. The increase of the boundary layer thickness as well as the increase of the shape factor for the downstream sensor show the effect of boundary layer thickening due to the adverse pressure gradient. The outer velocity is reduced by the deceleration of the flow since its direction is opposed to the pressure rise.

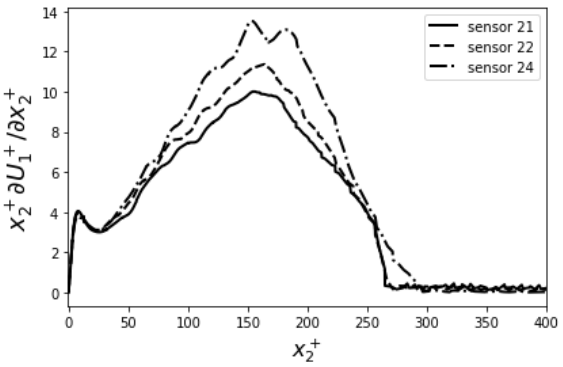

Figure 3.8: Normalised streamwise velocity gradient evolution in the normal-to-wall direction.

In Figure 3.9 (a), the normalised Reynolds stress components $\rho u_i' u_j'$ have been plotted as a function of x_2^+. i and j refer to the streamwise and normal-to-wall directions. The curve is normalised with inner scales: ρu_τ^2. A peak in Reynolds stress plot corresponds to a location of higher momentum transfer by fluctuating velocities. In this case, the APG modifies the peaks into a plateau which extends from the log-layer to the outer-layer ($8 \leq x_2^+ \leq 103$): the turbulent mixing is further increased. For ZPG cases, the maxima would

be in the viscous layer. It is reported in literature that the outer peak may be due to the hairpin structures developing away from the wall next to the TE (WU et al. 2019). Moreover, the anisotropy of the energy distribution among the stresses can be remarked. The normal-to-wall stress is systematically lower than the others (CHASSAING 2000).

The trend of viscous and turbulent shear stresses is plotted in Figure 3.9 (b). The red curve represents their sum, normalised by the wall shear stress. The viscous stress is dominant in proximity to the wall. Viscous and turbulent stresses are at the same level around $x_2^+ = 10$. Beyond this distance, Reynolds stresses become the main component of the shear stress. The maximum of the total stress curve and the extensions of its platform shape mainly depends on the Reynolds number of the flow (CHASSAING 2000). Eventually, sensor 22 proves a higher level of turbulence with respect to sensor 21 in both figures.

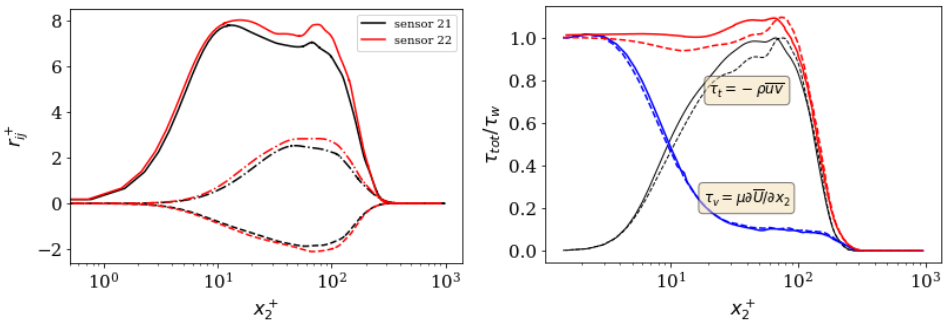

(a) (b)

Figure 3.9: (a) Reynolds stress components: r_{11} (solid line), r_{12} (dashed dotted line), r_{22} (dashed line). (b) Shear stress decomposition for sensor 21 and 22.

3.4 Analysis of velocity and wall-pressure fluctuations

3.4.1 NS-DNS turbulence statistics

The turbulence statistics can be quantitatively analysed by simultaneously observing the velocity fluctuations at two neighbouring points in the flow field. Velocity fluctuations beneath a turbulent boundary layer in the presence of an APG are investigated in this section. This has been achieved through two-points statistics for three sensors on the suction side of the airfoil (sensor 21, 22 and 24, Figure 3.2). A particular focus is made on the normal-to-wall velocity correlation coefficient R_{22}, since the cross-correlation S_{22} presented in (2.32) is its double spatial Fourier transform. The R_{22} profiles of two different sensors on the suction side of the airfoil will be compared. Moreover, the evolution of the correlation length and of the anisotropy coefficient in the normal-to-wall direction are discussed. Python codes have been used for post-processing.

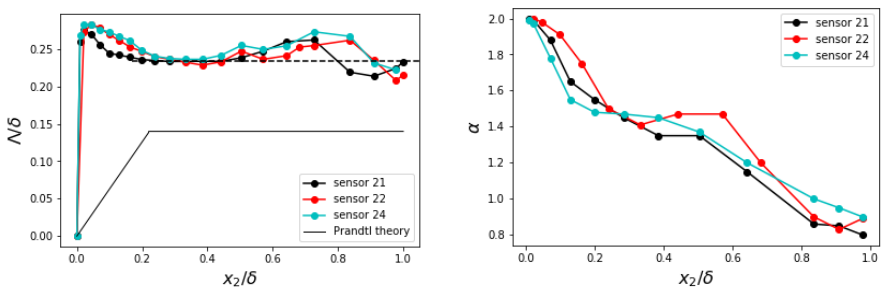

(a) (b)

Figure 3.10: (a) Normalised longitudinal velocity correlation coefficient and (b) anisotropy coefficient for two sensors on the suction side of the CD airfoil.

Analytical methods based on Panton&Linebarger's work involve the variation of the longitudinal length scale Λ_1 as a function of the distance from the wall and of the wavenumber in order to compute ϕ_{22}. In the present work, only the dependence from x_2 will be addressed. In Figure 3.10 (a), the longitudinal length scale is plotted for two sensors on the CD airfoil surface as in (2.5). The trend of Λ_1 according to Prandtl's theory is plotted too (PANTON and LINEBARGER 1974):

$$\Lambda_1 = \begin{cases} 0.63 x_2 \delta & x_2/\delta \leq 0.22 \\ 0.14\delta & x_2/\delta > 0.22 \end{cases} \tag{3.3}$$

Λ_1 increases along the normal-to-wall direction in the boundary layer. Since this quantity is related to the size of eddies, the reason of this trend may be the presence of bigger turbulent structures away from the wall. Moreover, the average value of its plateau proves higher than the theoretical one. The precise methodology for the calculation of turbulence length scale is still an open issue. In this case, a trapezoidal numerical method has been used for the integration. In order to avoid the negative lobes of $F(r)$, the integration interval is defined up to separations resulting in $F(r) > 0$.

The trend of the boundary layer anisotropy in the normal-to-wall direction is addressed in Figure 3.10 (b). This parameter is used as a scale coefficient for the longitudinal separation r_1 in order to collapse the curves of $R_{22}(r_1)$ and $R_{22}(r_3)$ in Figure 3.11 (see (2.6)). In the presence of an adverse pressure gradient, strong anisotropy is dominant only close to the surface, as in (KROGSTAD and SKARE 1995). Indeed, for low x_2^+ the two plots show the largest gap.

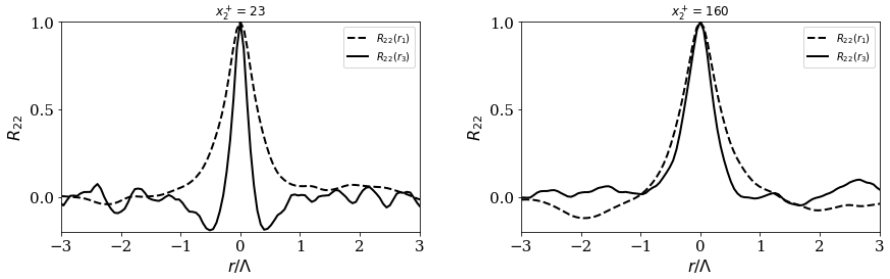

(a) $x_2^+ = 23$ (b) $x_2^+ = 160$

Figure 3.11: Vertical velocity correlations calculated for streamwise (r_1) and spanwise (r_3) directions for two different planes, sensor 21.

As demonstrated through the Lumley map in (WU 2019), the most severe departure from the 3D isotropy is for locations close to the wall. There the boundary layer is only 2D isotropic ($\alpha = 2$), while it tends to 3D isotropy ($\alpha = 1$) approaching to the external free-flow. The maximum of isotropy would be in absence of the airfoil surface then in this case at the farthest distance from it, where there is no shear influence. The plateau in the plot of α in the log-law region may be due to the enhanced mixing in the case of APG.

In Figure 3.12, Λ_1 is used to normalise the streamwise and spanwise separations of three different normal-to-wall layers. The longitudinal velocity correlation $F(r)$ is plotted as a function of streamwise separations. The reference point is the most upstream one in the considered volume, whereas the vertical velocity correlation coefficient is computed with respect to a reference point located at the centre of the volume. It is plotted against

spanwise separations for three planes parallel to the suction side of the airfoil. Negative lobes are present in the $R_{22}(r_3)$ plot for low x_2^+. These can be interpreted as an ascending and descending return flow on a large scale (CHASSAING 2000). On the contrary, for greater values of x_2^+, the increased size of eddies does not allow a similar recirculation. In the case of sensor 22, located downstream sensor 21, the correlation plot is more antisymmetric. Results for sensor 24 are not reported here for brevity since they follow the same trend.

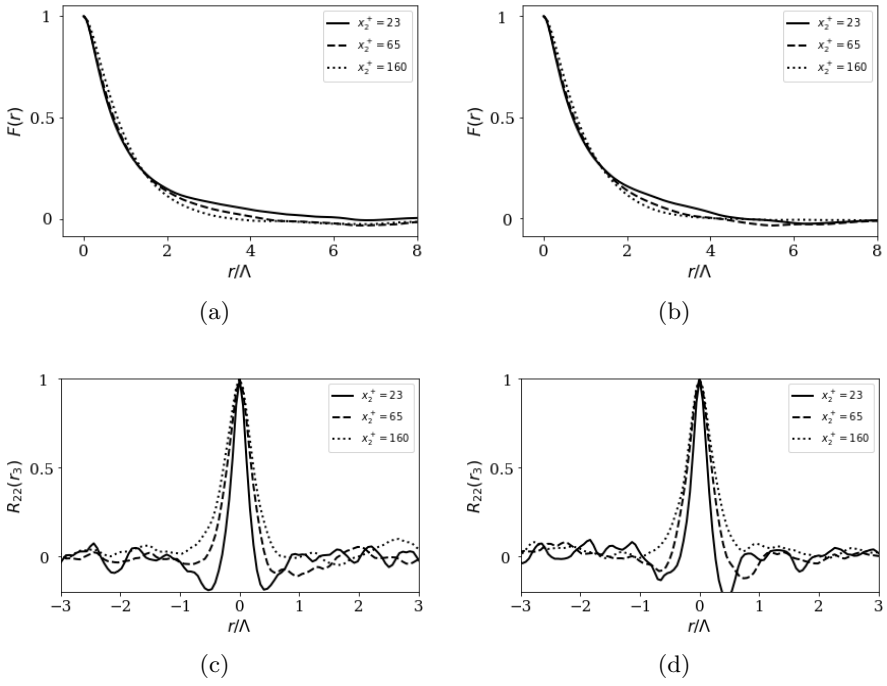

Figure 3.12: Longitudinal and vertical velocity correlations for sensor 21 (a,c) and 22 (b,d) for three different vertical positions.

A comparison between the models for $F(r)$ and Λ presented in Table 2.1 and the vertical velocity correlation of DNS data is depicted in Figure 3.13 for sensor 21. The results are computed on a plane at about half of the available volume, at $x_2^+ = 90$. Similar results were found for different positions in the normal-to-wall direction. As already discussed by (GRASSO et al. 2019), the models which fit R_{22} data the best are RDT and Lieppman's. While Lieppman's is in close agreement with numerical data for separations smaller than unity, RDT captures better the negative lobes of the curve. The Gaussian model is found to overestimate the numerical curves.

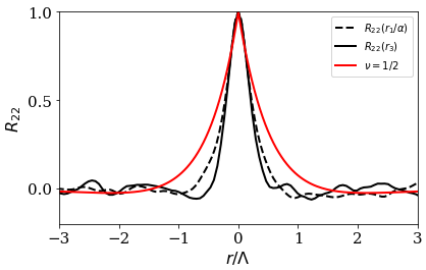

(a) Lieppman's model

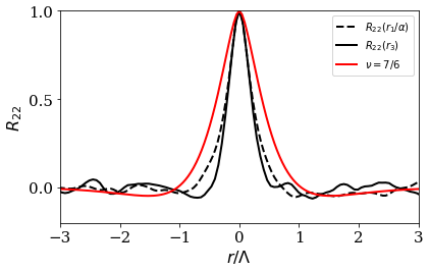

(b) RDT model

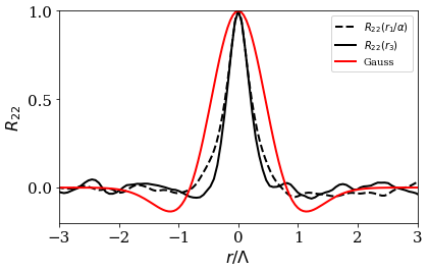

(c) Gaussian model

Figure 3.13: Comparison between models and measured vertical velocity correlations for $x_2^+ = 90$ for sensor 21. $\alpha = 1.4$ has been used to collapse $R_{22}(r_1)$ and $R_{22}(r_3)$.

3.4.2 Comparison with LBM-DNS data

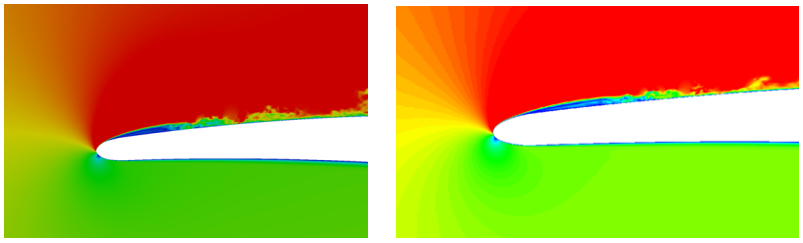

(a) (b)

Figure 3.14: Zoom on the TE recirculation bubble for (a) NS-DNS and (b) LBM-DNS, velocity magnitude contours.

This section focuses on the comparison between velocity correlations computed with NS-DNS and LBM-DNS data for sensor 22. In Figure 3.15, a slight difference between the two velocity profiles can be noticed, with the same trend remarked in (WU 2019). The boundary layer is thinner in LBM-DNS case: this is due to a slightly thinner TE recirculation bubble than the NS-DNS case, as it can be seen on the pressure coefficient plot in Figure 3.6 and on the velocity contours of Figure 3.14. The shape factor remains almost the same in both cases (Table 3.2).

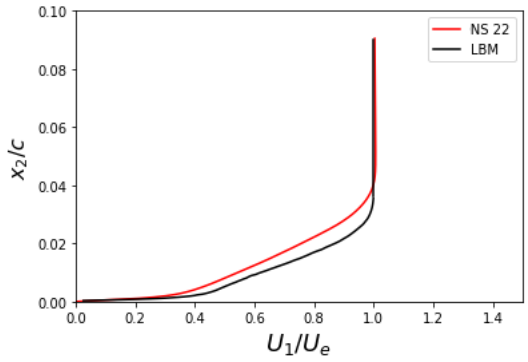

Figure 3.15: Comparison between NS-DNS and LBM-DNS velocity profile for sensor 22.

	LBM	DNS
δ_{p99} [mm]	4.69	4.94
H	1.76	1.89
U_e [m/s]	18.2	17.40

Table 3.2: NS-DNS and LBM-DNS boundary layer integral parameters.

The advantage of LBM simulation being its computational speed, it is easier to achieve a large physical time with respect to traditional Navier-Stokes solvers. In order to evaluate the convergence of the velocity correlation parameters, the post-processing has been performed for a a physical time of $\Delta t \sim 0.069\ s$ and $\Delta t \sim 0.136\ s$, which correspond to 8 and 16 flow-through times. The comparison of the two Δt is plotted in Figure 3.16. A negligible difference can be remarked in terms of longitudinal and vertical velocity correlations. Consequently, only the data for $\Delta t \sim 0.069\ s$ is considered in the following.

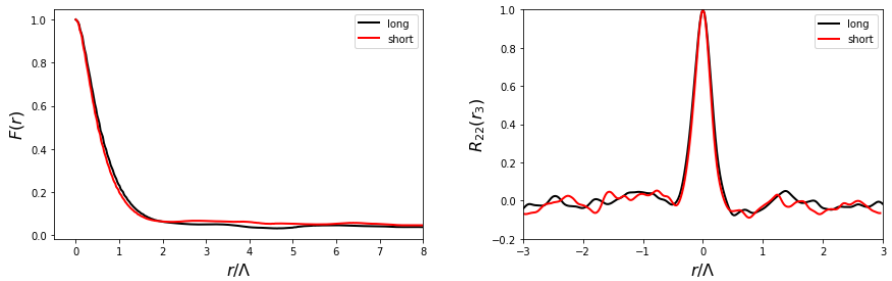

(a) (b)

Figure 3.16: Comparison between LBM-DNS results for 8 (red curve) and 16 (black curve) flow-through times.

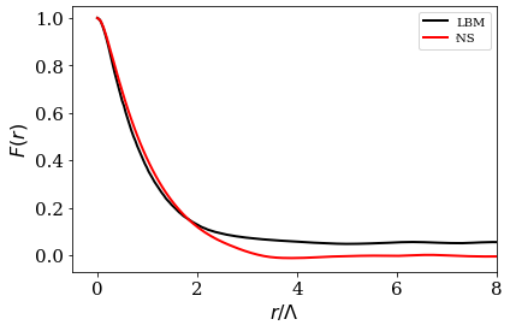

Figure 3.17: Longitudinal velocity correlation for sensor 22, comparison between NS-DNS and LBM-DNS data.

As shown in Figure 3.17, the longitudinal correlation function is not going to zero for large separations. This may be due to numerical errors caused by the interpolation of data. Since in LBM-DNS, the voxels do not perfectly follow the airfoil shape and their sides cross it, an interpolation must be made to impose the presence of the profile in the domain. For this reason, a great difference can be remarked between the longitudinal Taylor scale computed for the two different simulations: $F(r)_{LBM}$ not going to

zero. In order to overcome the problem, the integration of $F(r)_{LBM}$ has been truncated for the separation considered in the analysis of the corresponding layer in NS-DNS. As shown in Figure 3.18 (a), this method proves efficient only for the near-to-wall region of boundary layer, where Λ for the two simulations is comparable. At a farther distance from the wall, Λ_{LBM} trend diverges to higher values than in NS-DNS case. In (b), the anisotropy coefficient α has been plotted for the two simulations. The normal-to-wall evolution proves the same. The slight shift of the plot is due to the different height of the boundary layer in the two configurations.

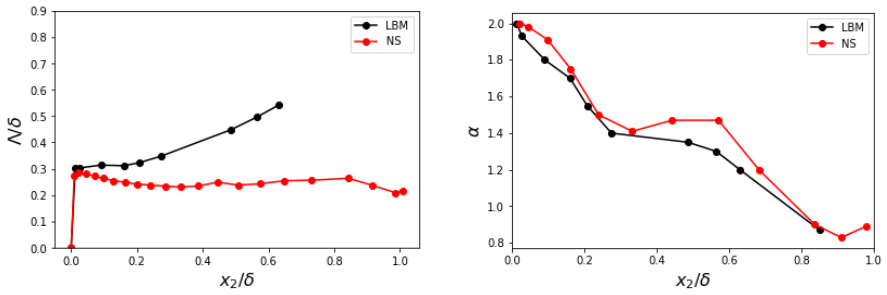

(a) $x_2^+ = 6$ (b) $x_2^+ = 130$

Figure 3.18: (a) Longitudinal length scale and (b) anisotropy coefficient for LBM-DNS and NS-DNS data of sensor 22.

In Figure 3.19, vertical velocity correlation is plotted for the two simulation techniques against spanwise separations. The reference point at the centre of the domain is the same for LBM-DNS and NS-DNS. Both at a small and at a large distance from the wall, an overall agreement between the results of the two simulations can be found. LBM-DNS simulation data capture well the peak and the correlation negative lobes. However, a small difference is remarked in the symmetry of the lobes of the R_{22} curves. As far as the relation between $R_{22}(r_1)$ and $R_{22}(r_3)$, LBM-DNS data showed the same trend as NS-DNS (Figure 3.11) as we can see in the evolution of α. The plots are not reported here for brevity.

A comparison between the longitudinal and vertical velocity correlations is made at several normal-to-wall positions of the boundary layer in the plane (r_1, r_2) (see Figure 3.20 and 3.21). While approaching to the outer part of the boundary layer, $R_{11}(r_1, r_2)$ contours appear to be tilted to the flow direction. The vortex stretching due to the mean shear causes an inclination of the structures towards the wall. This phenomenon is opposed to the increase in induced velocity that each limb of the hairpin structure of eddies imposes on the other. On the contrary, $R_{22}(r_1, r_2)$ is aligned almost vertically at every position in the boundary layer.

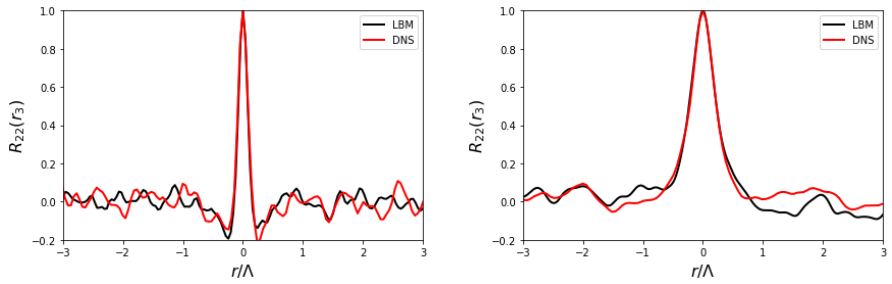

(a) $x_2^+ = 6$ (b) $x_2^+ = 130$

Figure 3.19: Comparison between NS-DNS and LBM-DNS data for sensor 22. The indicated x_2^+ values refer to NS-DNS boundary layer.

The wavelet approach made by (KROGSTAD and KASPERSEN 2002) explained this with a velocity fluctuation analysis. The inclination of turbulent structures depend on their associated length scale. Small-scale motion is theoretically vertical while larger scales are tilted to the wall. The major contributions to $\overline{v^2}$ are at a higher wavenumber (corresponding to a smaller structure scale) than for $\overline{u^2}$. Therefore the most important contributions to $R_{22}(r_1, r_2)$ are from little wavelet scales, characterised by a small amount of stretching and then vertical.

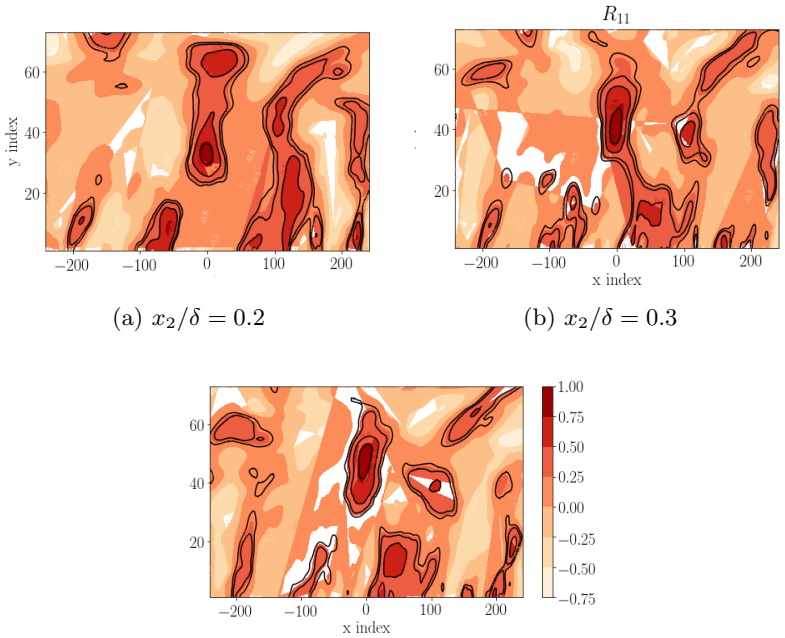

(a) $x_2/\delta = 0.2$

(b) $x_2/\delta = 0.3$

(c) $x_2/\delta = 0.45$

Figure 3.20: $R_{11}(r_1, r_2)$ contours made with LBM data from sensor 22. Contour levels: 0.1, 0.2, 0.3, 0.5, 0.8.

Eventually, $R_{22}(r_1, r_3)$ contours have been plotted on several planes parallel to the surface of the airfoil. Structures of increasing size can be identified for locations departing from the wall (see Figure 3.22). The stretching of vortices along the spanwise direction increases for locations far from the wall. This underlines once more the impossibility to exploit an isotropic model.

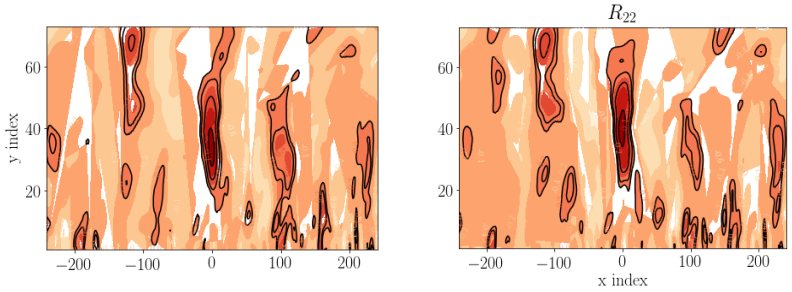

(a) $x_2/\delta = 0.2$ (b) $x_2/\delta = 0.3$

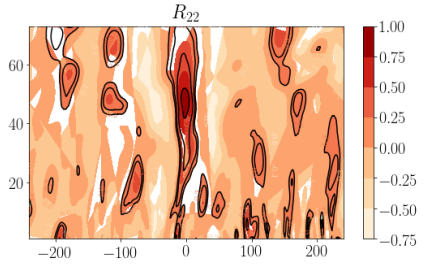

(c) $x_2/\delta = 0.45$

Figure 3.21: $R_{22}(r_1, r_2)$ contours made with LBM data from sensor 22. Contour levels: 0.1, 0.2, 0.3, 0.5, 0.8.

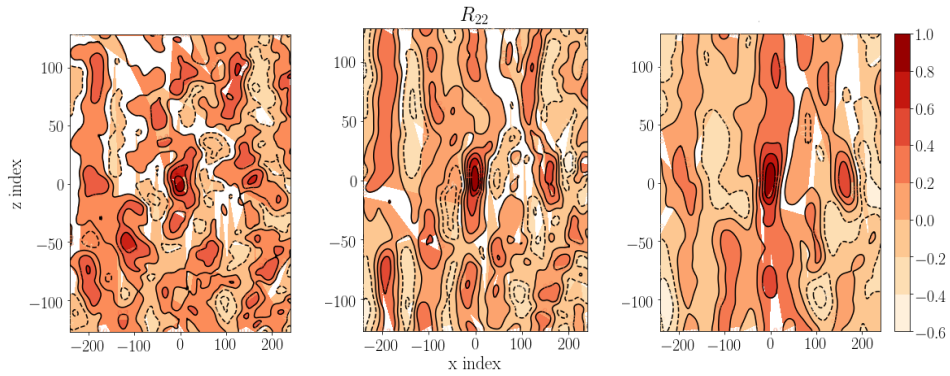

(a) $x_2/\delta = 0.6$ (b) $x_2/\delta = 0.8$ (c) $x_2/\delta = 0.95$

Figure 3.22: $R_{22}(r_1, r_3)$ contours made with LBM-DNS data from sensor 22. The location of the chosen plan is for increasing x_2^+ from (a) to (c). Contour levels: -0.2, -0.1, 0.1, 0.2, 0.3, 0.5, 0.8. The dashed lines correspond to negative values.

3.4.3 Wavenumber-frequency spectra

The properties of wall-pressure fluctuations both in space and in time can be expressed in terms of wavenumber-frequency spectrum. Several models for this spectrum have been proposed, mainly dealing with zero pressure gradient boundary layers. Different regions can be defined for the pressure wavenumber-frequency spectrum: $\Phi_{pp}(k_x, k_z, \omega)$. Firstly, the supersonic region for $k \leq k_a = 2\pi f/c_0$, the acoustic wavenumber, which represents the compressibility effects. Then the sub-convective region, $k_a \leq k \leq k_c$, a convective peak centred around the convective wavenumber $k_c = 2\pi f/U_c$ and the viscous region for $k \geq k_a$. U_c is the convection velocity, c the sound velocity and ω the radian frequency.

The convective peak is dominant and the most energetic. It represents the hydrodynamic signature of turbulent structures convected by the flow in the boundary layer. The pressure levels of the convective region are approximately 40 dB above the levels in the subconvective range for an attached turbulent boundary layer with zero pressure gradient. The acoustic and convective wavenumbers are related by:

$$k_a = Mk_c \tag{3.4}$$

where M is the free-stream Mach number.

This report focuses on two different signal processing methods for sensor 22, proposed by (COHEN and GLOERFELT 2018) and (SALZE et al. 2014). Applying Salze's post-processing, a simple fast Fourier transform $\hat{p}(k, \omega)$ of the pressure field is performed. A Welch's algorithm is applied for the time dimension: three overlapping segments are considered from the total of the samples, stored every 200 iterations of the DNS. Each segment is weighted by a Hann window to reduce the creation of new frequency components (spectral leakage). The sampling frequency is 666 Hz. Under the assumption of stationary random signals and ergodicity (the time average must be the same as the ensemble average), the cross spectral density is defined as

$$R_{pp}(\mathbf{x}, \mathbf{r}, \omega) = \lim_{T \to \infty} \frac{2\pi}{T} E[\hat{p}(\mathbf{x} + \omega)\hat{p}^*(\mathbf{x} + \mathbf{r}, \omega)] \tag{3.5}$$

A Fourier transform in space will then provide the wavenumber-frequency spectrum:

$$\varphi_{pp}(\mathbf{k}, \omega) = \frac{1}{(2\pi)^2} \int \int R_{pp}(\mathbf{r}, \omega) e^{-i\mathbf{k}\cdot\mathbf{r}} d\mathbf{r} \tag{3.6}$$

In Cohen's method, a fast Fourier transform is applied in the spanwise direction. Then the Welch's algorithm is implemented in time with Hann windowing. The main difference from Salze is the Capon's spectral estimator. Conventional methods of spectrum estimation employ a fixed wavenumber

windows. This high-resolution method of estimation employs a wavenumber window whose shape changes as a function of the wavenumber at which an estimate is obtained (CAPON 1969). The estimator is eventually exploited to enhance the resolution along the streamwise direction:

$$\hat{P}_{Capon}(\omega, k_x, k_z) = \frac{n_x + 1}{e^H(k_x) R_{pp}^{-1}(\omega, k_z) e(k_x)} \tag{3.7}$$

where $e(k_x)$ is the steering vector and R_{pp}^{-1} the inverse of the auto-correlation matrix.

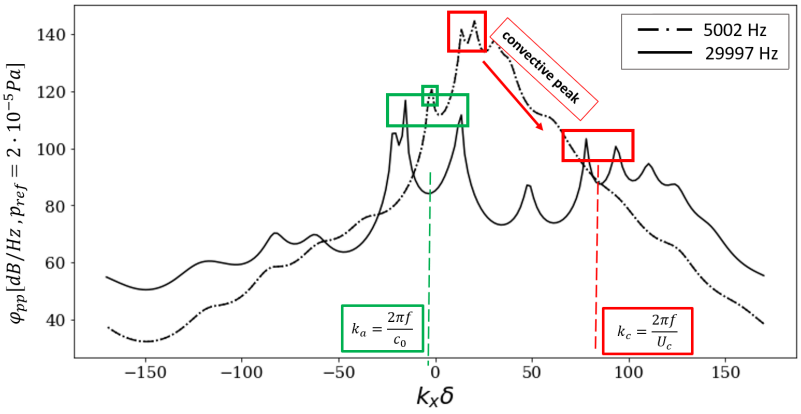

(a)

Figure 3.23: Wavenumber-frequency spectra for increasing frequencies (green: acoustic component; red: convective component).

As we can see in Figure 3.23, at low frequencies $k_x = k_a \sim k_c$: the convective contribution (red box) is dominant and the acoustic part (green box) can hardly be identified. At higher frequencies, the two contributions separate and the acoustic part becomes non negligible with respect to the hydrodynamic one. As remarked by (COHEN and GLOERFELT 2018), the acoustic levels tend to increase in the case of adverse pressure gradient.

Iso-contours of $\varphi_{pp}(\omega, k_x, k_z)$ in the (k_x, k_z) plane are plotted in Figure 3.24 for both cases of low and high frequencies. The convective ridges look like an elongated elliptical shape centred on k_c, whose major axis is in the spanwise direction. According to literature, the aspect ratio of the elliptical shape is lower for APG cases (SALZE et al. 2014). The convective wavenumber is shifted towards higher positive streamwise wavenumbers as the frequency increases and the φ_{pp} level of the convective ridge decreases. The acoustic domain is contained in the ellipse of equation:

$$\left(k_x + \kappa_0 M/\beta^2\right)^2 / \left(\kappa_0/\beta^2\right)^2 + k_z^2 / \left(\kappa_0/\beta\right)^2 = 1 \qquad \beta = \sqrt{1 - M^2} \tag{3.8}$$

which is plotted with a white dashed line. For low frequencies, the ellipse and the convective ridge are almost superimposed, whereas for high frequency they can be distinguished neatly.

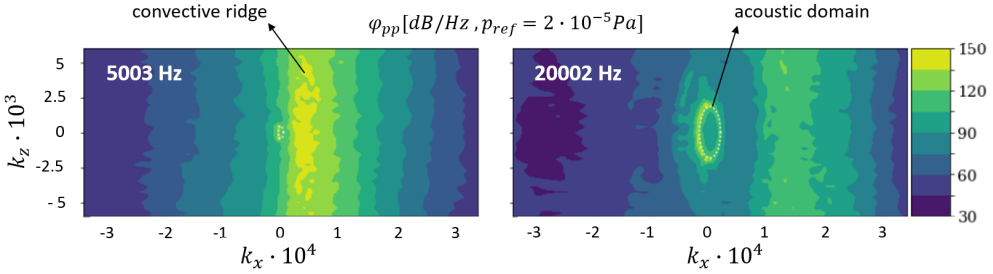

Figure 3.24: Comparison between wavenumber- frequency spectra for low and high frequencies in the (k_x, k_z) domain.

Eventually, in Figure 3.24 the wall-pressure spectrum has been plotted in the (k_x, ω) domain with Cohen and Salze's methods. The reduced spectral noise thanks to Capon's filtering can be appreciated. The white dashed lines represent the estimations of the convective velocity $U_c = nU_0$ propagating downstream, with $n = 0.6$, 0.7 and 0.8. The dotted lines represent the acoustic velocity. As it can be seen from their slope towards negative longitudinal wavenumbers, acoustic waves are mainly propagating upstream. This is due to the low Mach number configuration.

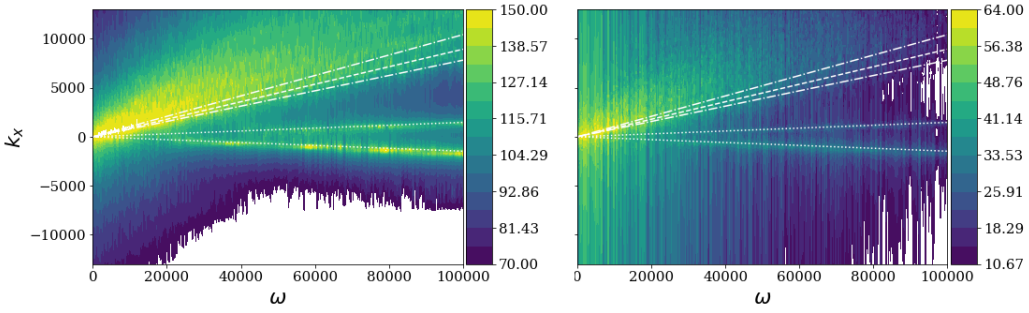

Figure 3.25: Wall-pressure spectrum in the (k_x, ω) domain: (right) Salze's method, (left) Capon's filtering.

3.4.4 Prediction of the wall-pressure power spectral density function

In order to compute wall-pressure PSD (2.32), a multi-dimensional integration must be performed. Monte Carlo integration methods have been used in this work. This technique allows the number of samples of the integrand function and the rate of convergence of the estimation of the integral to be independent of the number of dimensions.

Monte Carlo method

A Monte Carlo technique is any technique making use of random numbers in order to solve a problem. Historically, the first large-scale calculations which exploited the Monte Carlo method were neutron studies, random processes for which the employ of random numbers is natural. The applicability of the method depends on the ability of the user to formulate the problem in such a way that random numbers may be used to obtain the solution. The Monte Carlo result f is an estimator of the integral

$$I = \int_0^1 \dots \int_0^1 f\left(x_1, x_2, \dots, x_n\right) \mathrm{d}x_1 \mathrm{d}x_2 \dots \mathrm{d}x_n \tag{3.9}$$

According to the law of large numbers, the sum of the evaluations of a probability density function $f(u_i)$ on an interval from a to b, divided by the amount N of random numbers u_i, will converge to the expectation of the function f. Hence, as n becomes very large:

$$\langle \tilde{f} \rangle = \frac{1}{N} \sum_{i=1}^{n} f\left(u_i\right) \rightarrow \frac{1}{b-a} \int_a^b f(u) \mathrm{d}u \tag{3.10}$$

The mathematical properties of a Monte Carlo technique are the following:

- If the variance of f is finite, the Monte Carlo estimate converges to the true value of the integral for very large n.
- The expectation of the Monte Carlo estimate is the true value of the integral.
- The Monte Carlo estimate approaches a Gaussian distribution.
- The standard deviation of the Monte Carlo estimate is given by:

$$\epsilon = \mathcal{O}\left(\sqrt{\frac{\mathrm{Var}(\langle \tilde{f} \rangle)}{N}}\right) \qquad \mathrm{Var}(\langle \tilde{f} \rangle) = \frac{\mathrm{Var}(f)}{N} \tag{3.11}$$

The application of this algorithm requires a random numbers generator. However, deterministic computers can provide, at best, Quasi-Random numbers to sample the integral. Hence, this standard Monte Carlo algorithm is named Quasi-Uniform sampling.

A different technique to apply the Monte Carlo method is the *recursive stratified sampling*. The computational volume is split in two parts, with N_a and $N - N_a$ points each. In this case, the estimator f becomes:

$$\langle \tilde{f} \rangle' = \frac{1}{2}\left(\langle \tilde{f} \rangle_a + \langle \tilde{f} \rangle_b\right) \qquad \mathrm{Var}\left(\langle \tilde{f} \rangle'\right) = \frac{1}{4}\left(\frac{\mathrm{Var}_a(f)}{N_a} + \frac{\mathrm{Var}_b(f)}{N - N_a}\right) \tag{3.12}$$

Its variance is minimised when:

$$\frac{N_a}{N} = \frac{\sigma_a}{\sigma_a + \sigma_b} \quad \longrightarrow \quad \mathrm{Var}\left(\langle \tilde{f} \rangle'\right) = \frac{(\sigma_a + \sigma_b)^2}{4N} \tag{3.13}$$

where $\sigma = \sqrt{\mathrm{Var}(\langle \tilde{f} \rangle)}$. The variance in this case is never greater than the variance computed by the standard Monte Carlo method. A fixed number of function evaluations N is allocated at the beginning of the execution, then each dimension of integration is divided in two sub-volumes. In each sub-volume, a fraction of the N samples is used to estimate the variance of f. The remaining points are allocated according to the equation (3.13). This method is implemented in MISER algorithm, available in the Scikit-Monaco Python package.

Another way to further reduce the variance and then accelerate the convergence of the integration if to apply the *importance sampling*. Importance sampling means choosing a good distribution from which to simulate one's random variables. A change in variable is introduced to flatten the function in the new co-ordinate system so that fewer samples are required to converge. The sample is drawn from a proposal distribution and the integral re-weighted using importance weights so that the correct distribution is targeted. The method can be defined as

$$E_f[h(\vec{X})] = \int_X h(x)g(x)dx \tag{3.14}$$

where h is some function and g is the PDF of x. $g(x)$ must be found to mimic $h(x)$. Another PDF $u(x)$ on the same domain is considered, such that $u(x) = 0$ implies $h(x)g(x) = 0$.

$$\int h(x)g(x)dx = \int \frac{h(x)g(x)}{u(x)}u(x)dx = E_u\left[\frac{h(\vec{X})g(\vec{X})}{u(\vec{X})}\right] \tag{3.15}$$

E_u is the expectation for a probability for which the distribution of $\vec{X}$ is $u(x)$ rather than $g(x)$. The density $g(x)$ is called the target distribution, $u(x)$

the proposal distribution and $g(x)/u(x)$ the likelihood ratio. The random samples are generated according to $u(x)$ distribution. The Monte Carlo estimator is

$$\langle \tilde{f} \rangle = \frac{1}{n} \sum_{i=1}^{n} \frac{h\left(\vec{X}_i\right) g\left(\vec{X}_i\right)}{u\left(\vec{X}_i\right)} \tag{3.16}$$

Application to the wall-pressure spectrum

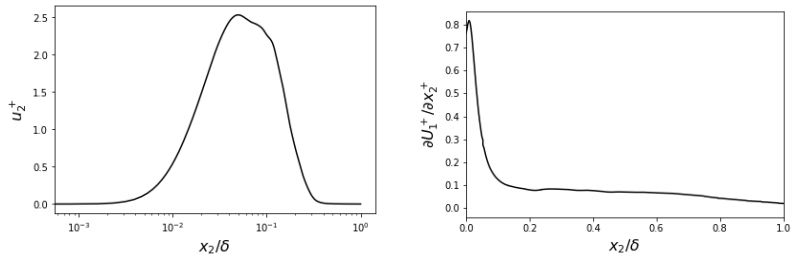

(a) (b)

Figure 3.26: (a) Normalised rms of vertical velocity fluctuations and (b) normalised streamwise velocity gradient for sensor 21.

Data from sensor 21 of NS-DNS is considered. The computation of φ_{pp} as in (2.32) requires several inputs:

- the root-mean-square (rms) of the normal-to-wall velocity fluctuations u_2' (Figure 3.26 (a))
- the mean streamwise velocity gradient profile $\partial U_1/\partial x_2$ (Figure 3.26 (b))
- the evolution of the longitudinal length scale in the normal-to-wall direction
- the evolution of the anisotropy coefficient α

Monte Carlo algorithm with a recursive stratified sampling technique has been used. Built-in Python libraries were exploited. A special focus is made on the role of boundary layer anisotropy. In section 3.4.1, the relation between the anisotropy coefficient and the vertical distance from the wall has been analysed. However, Panton&Linebarger theory (PANTON and LINEBARGER 1974) suggests that the influence of wavenumber on α should be accounted for when computing wall-pressure spectra. They calculated spectra for $\alpha = 1$, 2, and 3 and found that increasing the anisotropy factor

increases the level of the spectrum and shifts it to lower wave numbers. A model based on this concept is Remmler's (REMMLER et al. 2010) :

$$\alpha = \begin{cases} 3 & k_1\delta < 1 \\ \text{linear decrease} & 1 \leq k_1\delta \leq 5 \\ 1 & k_1\delta > 5 \end{cases} \tag{3.17}$$

which states that high wave number structures tend more to the isotropic behaviour.

In the present study, a comparison was made between spectra computed with a fixed α and a variable $\alpha = f(x_2)$. The distribution of α for sensor 21 can be found in Figure 3.10 (b).

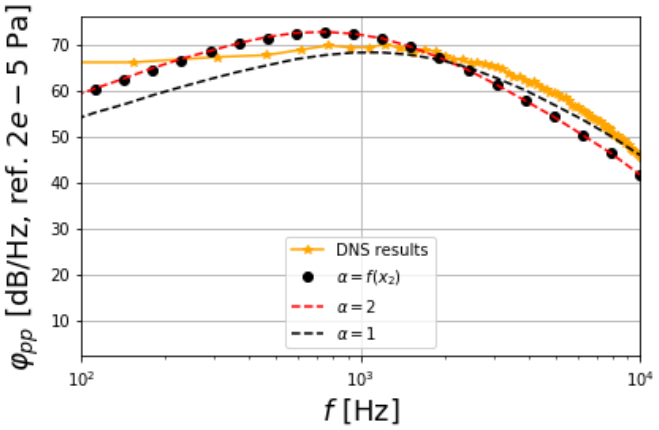

Figure 3.27: Wall-pressure PSD for sensor 21 computed with both fixed and variable anisotropy coefficient α. 100000 samples and 4 CPUs are used for the application of the Monte Carlo algorithm.

The integration boundaries of(2.32) are fixed to $X_2 \in [0, \delta_{p99}]$, $X_2' \in [0, \delta_{p99}]$ and $k_3 \in [0, 1000]$. The reference spectrum is the one directly computed with NS-DNS data. Pressure signals were recorded for 7 flow-through times at a sampling frequency of 78 kHz. As shown in Figure 3.27, the same trend remarked by Panton when the anisotropy coefficient increases is found. $\alpha = 3$ curve proves too high at low frequencies and underestimating the spectrum at high frequencies. The spectrum for $\alpha = 1$ is the one fitting NS-DNS data the most, especially at high frequencies. The spectrum calculated for a variable distribution of α totally superimpose to the one for $\alpha = 2$.

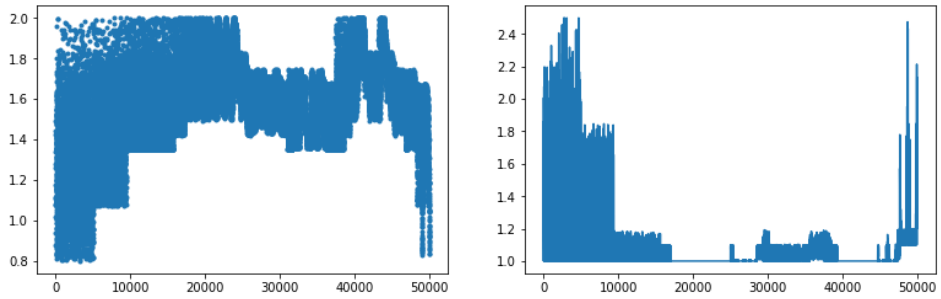

(a) (b)

Figure 3.28: Random throw of α for a CPU (50000 samples) for (a) the distribution of α shown in section 3.4.1 and (b) a different distribution with a plateau at $\alpha = 1$.

However, the perfect superimposition of the two curves is not considered as totally reliable. So as to check the random throw during the interpolation of α computed by the algorithm, two different distributions of $\alpha(x_2)$ have been tested. In Figure 3.28 (a), the random throw for a CPU for the distribution in Figure 3.10 (b) is shown for a population of 50000 samples (maximum value 2, minimum value 0.8, monotonically decreasing function). The random throw mean is around the mean between the extreme values of α. In Figure 3.28 (b), a distribution of α computed during previous research has been used. This latter is characterised by a plateau around the value $\alpha = 1$ and the maximum value is around 2.5. In this case, 80% of the random values is below 1.1. The random throw proves really sensitive to the distribution of the anisotropy coefficient. Furthermore, the bias in the throw may be due to both the choice of the sub-volumes in the important sampling and the exponential decrease in (2.32). Thus, a conclusion cannot be drawn about the superimposition of the two curves without further analysis.

The importance sampling method has been tested with the same input data for fixed values of the anisotropy coefficient. Non-parallel Fortran90 codes have been exploited. The obtained spectra are shown in Figure 3.29. This method shows the same trend of previous cases when the anisotropy coefficient increases. The curve computed with Remmler's method is superimposed with $\alpha = 1$ for medium to high frequencies. $\alpha = 1$ remains the value fitting DNS data the most. As far as the behaviour at high frequencies, the result is considered to be not consistent with the one obtained with the recursive stratified sampling. The curves for different values of the anisotropy coefficient coincide. Further investigations must be done to understand the reasons of this inconsistency.

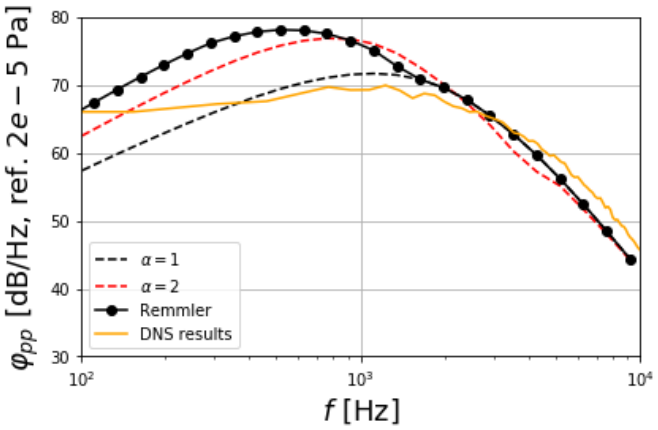

Figure 3.29: Wall-pressure PSD computed with the importance sampling method for the same airfoil. Comparison between fixed values of α and Remmler's model.

Conclusion and perspectives

This report sums up the state-of-the-art and the necessary prerequisites within the framework of this internship. A brief overview of homogeneous turbulence and acoustic analogies is given, with a focus on current numerical techniques. The considered case study for a DNS simulation has been presented: a Controlled-Diffusion airfoil at an angle of attack of 8°. Two types of DNS simulation on the same profile have been addressed: a Navier-Stokes simulation and a simulation applying the Lattice-Boltzmann method. The post-processing focused on data from three sensors near the trailing edge on the suction side of the airfoil. The boundary layer has been analysed for both simulations and comparable results have been found. The only remarkable difference is the thickness of the leading edge recirculation bubble, thicker in the NS-DNS case.

Within the framework of Amiet's theory, statistical methods based on Panton and Linebarger's work have been exploited for modeling the source terms for wall-pressure spectrum predictions. The considered model is anisotropic. Turbulence statistics and boundary layer anisotropy have been investigated both for NS and LBM DNS. Comparable results have been found. The anisotropy is maximum near the wall due to the effect of shear and decreases in the outer region of the boundary layer.

Secondly, wavenumber-frequency spectra have been exploited to investigate the acoustic and hydrodynamic contributions on a large range of frequencies. As far as the power spectral density prediction for trailing-edge noise, two different Monte Carlo techniques have been used for the most upstream sensor. Previous research findings have been validated for the application of the recursive stratified sampling to the problem. The distribution of the anisotropy coefficient found during the analysis of turbulence statistics has been set as an input to the model and compared to fixed values of anisotropy. The choice of a fixed and unitary anisotropy coefficient gives the predicted spectrum which fits DNS data the most.

As a continuation of this internship work, three major aspects must be looked at. Firstly, as far as turbulence statistics, a more accurate way to compute the longitudinal length scale must be found. It would be in-

teresting to keep into account the turbulence-turbulence interaction term too. Secondly, the dependence of the boundary layer anisotropy both on the wavenumber and on the normal-to-wall location should be considered. Lastly, the efficiency of the application of recursive stratified sampling to the wall-pressure spectrum prediction must be evaluated. Further investigation of the importance sampling application will allow more reliable comparison between the two methods.

References

AMIET, R. K. (1975). "Acoustic radiation from an airfoil in a turbulent stream". In: *Journal of Sound and Vibration* 41.4, pp. 407–420.

— (1976). "Noise due to turbulent flow past a trailing edge". In: *Journal of Sound and Vibration*.

BAILLY, C. and G. COMPTE-BELLOT (2015). *Turbulence*. Springer.

CAPON, J. (1969). "High-Resolution Frequency-Wavenumber Spectrum Analysis". In: *Proceedings of the IEEE* 57.

CHASSAING, P. (2000). *Turbulence en mècanique des fluides*. Cépaduès-Editions.

COHEN, E. and X. GLOERFELT (2018). "Influence of pressure gradients on wall pressure beneath a turbulent boundary layer". In: *Journal of Fluid Mechanics* 838, pp. 715–758.

GOODY, M. (2004). "Empirical Spectral Model of Surface Pressure Fluctuations". In: *AIAA Journal* 42.9, pp. 1788–1794.

GRASSO, G. et al. (2019). "Analytical models of the wall-pressure spectrum under a turbulent boundary layer with adverse pressure gradient". In: *Journal of Fluid Mechanics*.

HOBBS, D. E. et al. (1984). "Development of Controlled Diffusion Airfoils for Multistage Compressor Application". In: *Journal of Engineering for Gas Turbines and Power* 106.

HOWE, M. S. (1978). "A Review of the Theory of Trailing Edge Noise". In: *Journal of Sound and Vibration* 61.3, pp. 437–465.

HU, N. and M. HERR (2016). "Characteristics of wall pressure fluctuations for a flat plate turbulent boundary layer with pressure gradients". In: *22nd AIAA/CEAS Aeroacoustics Conference*.

KRAICHNAN, R. H. (1956). "Pressure field within homogeneous anisotropic turbulence". In: *Journal of the Acoustical Society of America* 28.1, pp. 64–72.

KROGSTAD, P.-A. and J.H. KASPERSEN (2002). "Structure inclination angle in a turbulent adverse pressure gradient boundary layer". In: *Journal of Fluids Engineering*.

KROGSTAD, P.-A. and P.E. SKARE (1995). "Influence of a strong adverse pressure gradient on the turbulent structure in a boundary layer". In: *Physics of Fluids*.

LEE, S. (2018). “Empirical Wall-Pressure Spectral Modeling for Zero and Adverse Pressure Gradient Flows”. In: *AIAA Journal* 56.5.

MINCU, D.C. and E. MANOHA (2014). “Numerical and Experimental Characterization of Fan Noise Installation Effects”. In: *Journatl Aerospace Lab* 7.

PANTON, R. L. and J. H. LINEBARGER (1974). “Wall pressure spectra calculations for equilibrium boundary layers”. In: *Journal of Fluid Mechanics* 65.2, pp. 261–287.

POPE, S.B. (2000). *Turbulent Flows*. Cambridge.

REMMLER, E. et al. (2010). “Computation of Wall-Pressure Spectra from Steady Flow Data for Noise Prediction”. In: *AIAA JOURNAL* 48.

ROGER, M. (2013). “Noise Sources in Turbulent Shear Flows: Fundamentals and Application”. In: Springer. Chap. Broadband Noise from Lifting Surfaces Analytical Modeling and Experimental Validation, pp. 289–344.

ROGER, M. and S. MOREAU (2004). “Broadband Self-Noise from Loaded Fan Blades”. In: *AIAA Journal* 42.3, pp. 539–544.

— (2005). “Back-scattering correction and further extensions of Amiet’s trailing-edge noise model. Part 1: theory”. In: *Journal of Sound and Vibration* 286.3, pp. 477–506.

— (2009). “Back-scattering correction and further extensions of Amiet’s trailing-edge noise model. Part II: Application”. In: *Journal of Sound and Vibration* 323.1-2, pp. 397–425.

— (2012). “Addendum to the back-scattering correction of Amiet’s trailing-edge noise model”. In: *Journal of Sound and Vibration* 331.24, pp. 5383–5385.

ROZENBERG, Y. et al. (2012). “Wall-pressure spectral model including the adverse pressure gradient effects”. In: *AIAA Journal* 50.10, pp. 2168–2179.

SALZE, E. et al. (2014). “An experimental characterisation of wall pressure wavevector-frequency spectra in the presence of pressure gradients”. In: *20th AIAA/CEAS Aeroacoustics Conference*.

SANDBERG, R. et al. (2008). “Direct numerical simulations of noise generated by turbulent flow over airfoils.” In: *14th AIAA/CEAS Aeroacoustics Conference*.

SANJOSE, M. and S. MOREAU (2011). “Direct self-noise simulation of the installed Controlled Diffusion airfoil”. In: *AIAA Journal*.

SLAMA, M. et al. (Apr. 2018). “A Kriging-based elliptic extended anisotropic model for the turbulent boundary layer wall pressure spectrum”. In: *Journal of Fluid Mechanics* 840, pp. 25–55.

WILSON, D. K. (1998). *Turbulence Models and the Synthesis of Random Fields for Acoustic Wave Propagation Calculations:* tech. rep. Fort Belvoir, VA: Defense Technical Information Center.

WU, H. (2019). “Direct Numerical Simulation of Airfoil Self-Noise at High Reynolds Numbers”. PhD thesis. Université de Sherbrooke.

WU, H. et al. (2019). “Effects of pressure gradient on the evolution of velocity-gradient tensor invariant dynamics on a controlled-diffusion aerofoil at Re=150000”. In: *Journal of Fluid Mechanics* 868, pp. 584–610.

Glossary

α	anisotropy coefficient
β_c	Clauser's parameter
c_0	sound velocity
c_f	skin friction coefficient
c_p	pressure coefficient
δ	boundary layer thickness
δ^*	boundary layer displacement thickness
Γ	Gamma function
G	Green's function
Φ_{pp}	power spectral density of wall-pressure fluctuations
$f(r)$	longitudinal correlation function
$g(r)$	transverse correlation function
K_ν	modified Bessel function
k	wavenumber
Λ	turbulence length scale
λ	wavelength
L	characteristic length scale
l_z	fluctuations transverse coherence length
μ	dynamic viscosity
ν	parameter for Von Karman's model
θ	boundary layer momentum thickness
P_e	free field pressure
p'	pressure fluctuations
R_{ij}	correlation coefficient
Re	Reynolds number
ρ	flow density
ρ'	density fluctuations
S_{22}	normalised cross-spectrum of vertical velocity fluctuations
S_{pp}	noise spectrum
σ	variance
U^+	normalised streamwise velocity
U_e	free field velocity
U_c	convection velocity
u_τ	friction velocity
$u',\ v', w'$	velocity fluctuations
T_{ij}	Lighthill's stress tensor
τ_w	wall shear
$x_1,\ x_2, x_3$	streamwise, normal-to-wall and spanwise Cartesian coordinates
x_2^+	normalised normal-to-wall position
ω	angular frequency